

Dwight L. Jaggard, Aaron D. Jaggard, and Panayiotis V. Frangos

ABSTRACT

We provide a selected review of *fractal electrodynamics* by investigating the nature of electromagnetic wave interactions with fractal surfaces and superlattices. Of particular interest are the ways in which these fractal objects imprint their characteristic geometry on scattered waves and the physical basis and explanation for these interactions. We review fractal geometry, sets, and descriptors with an emphasis on the roles of dimension and lacunarity.

Since multiscale rough surfaces are often modeled by fractals, we examine here the scattering from simple fractal surfaces as a function of roughness and scattering angle using both the Kirchhoff approximation and the T-matrix approach. We find a simple relation between fractal dimension and variations in scattering cross section for small or moderate roughness. For increasing roughness we observe the role of polarization.

Next, we formulate and examine the reflection characteristics of multiscale layered media and investigate the physical explanation for the distinctive and complex reflection characteristics from these superlattices as a function of both frequency and variation in fractal descriptors. Physically motivated models of interference provide a fundamental understanding of the reflection data as contained in *twist plots*. We review recent methods of extracting fractal descriptors from superlattice scattering data using both frequency-domain and time-scale techniques.

1.1 INTRODUCTION

1.1.1 Background

Fractal electrodynamics grew from the electromagnetics research of the past several decades that examined the blending of wave concepts and fractal geometry [1–4]. The goal of this work has been to study and understand the effect of canonical multiscale structures on the scattering, radiation, and guiding of electromagnetic waves in much the same way that the effect of simple Euclidean shapes on electromagnetic waves has been studied since the late nineteenth century. Several researchers examining scattering phenomena, circa 1980, found that in select cases the fractal dimension was encoded in the scattered wave in an easily decipherable way. The intriguing possibility arose that this phenomenon might be characteristic of a large class of fractal scatterers illuminated by electromagnetic waves. In the mid-1980s we set out to see if this was so and if this knowledge could be used in electromagnetic applications. More recently we have been looking to see if other

fractal descriptors are similarly embedded in the scattering data and if these additional fractal attributes could aid in the synthesis of new devices and systems. To summarize some of these research results, we examine in this chapter two cases that are both straightforward to understand and physically illuminating—scattering from fractal surfaces and scattering from fractal superlattices.

Work in fractal electrodynamics builds on the initial literature on wave scattering and diffraction from fractal geometries starting with the pioneering work by Berry on *diffractals* [5], [6]; scattering from fractal surfaces and slopes by Jakeman [7–10]; initial studies of diffraction by fractal objects and apertures [11–21]; and X-ray, photon, and neutron scattering from fractal aggregates, colloids and porous media [22–33]. In addition, a number of books on fractals, several of which we note here [34–49], [78], provide a wealth of supporting material.

Although the primary goals of this chapter are to become familiar with fractals and waves, to analyze several canonical examples, and to understand their underlying physical principles, there are also a number of potential applications of this work. We envision these to include device synthesis for the microwave, millimeter wave, and optical regimes, as well as the use of fractals in remote sensing, characterization, and classification. Several examples of the synthesis problem are given in the following chapters where fractal antenna elements and arrays are considered.

1.1.2 Overview

We first introduce the fundamental concepts of fractal geometry, fractal sets and fractal descriptors. We examine the construction of statistical and more idealized fractals as well as the definition of the primary fractal descriptor, the *fractal dimension*. This is followed by an introduction to fractal texture through *lacunarity*, which provides a secondary fractal descriptor. We then briefly discuss the relationship between fractals and waves.

In the next section we investigate electromagnetic and optical wave scattering from fractally rough surfaces [7–10], [50–67]. Here we demonstrate the methods by which fractals imprint their distinctive geometry on interrogating waves to generate characteristic scattered waves. In all cases the spread of the scattered waves is related to surface roughness which can be quantified through fractal descriptors. We envision applications for this work that range from the radar and optical remote sensing of sea state to the characterization and classification of both natural and manufactured surfaces.

Finally, we investigate the reflection of electromagnetic and optical waves from fractal superlattices or multilayers [68–77]. We find that the superlattices also impress their fractal characteristics on scattered waves in quantifiable ways. We observe the symmetry of the superlattice structure in both the method of solution and the form of the scattering data. Of particular value is the use of *twist plots* to display frequency-domain results in an easily understandable way. Time-scale analysis using wavelets also provides insight into this scattering problem from an alternative and timely viewpoint. Potential applications of these results include the modeling and synthesis of resonant cavities, mirrors, multilayers and other devices for the microwave, millimeter wave, and optical wave regimes. In addition, our results have application to the analysis and modeling of wave propagation in finely divided layered media.

1.2 INTRODUCTION TO FRACTALS

A fractal is a shape made of parts similar to the whole in some way.
B. B. Mandelbrot [37]

Fractals allow us to describe the natural world according to *its* geometry. They appear irregular, yet have underlying order, and possess structure on all scales. It is not surprising, then, that the language of fractal geometry allows us to describe natural phenomena as diverse as fluid flow in porous materials and lightning strokes with greater ease than does Euclidean geometry.

Here we discuss some of the common characteristics of fractals, particularly their self-similarity and structure on all scales. It is these traits which make fractals, such as those in Fig. 1.1, useful for modeling naturally occurring structures, such as mountains. We also consider how one may describe a fractal using its fractal dimension, which need not be an integer, and its lacunarity, a more recently investigated means of quantifying the texture of a fractal set.

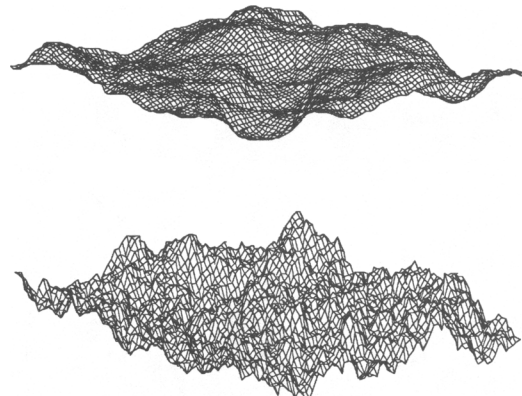


Figure 1.1 Fractal mountains including both a smoothly undulating (top) and a jagged and volume-filling (bottom) version. [Figure taken from “Scattering from Fractally Corrugated Surfaces,” D. L. Jaggard and X. Sun, J. Opt. Soc. Am. A, 7, 1131–1139 (1990). © 1990 Optical Society of America.]

1.2.1 What Are Fractals?

1.2.1.1 Fractal Characteristics

Although there are no strict guidelines as to what constitutes a fractal, there are a number of qualities which frequently characterize fractals. The first is self-similarity and structure at all scales. A coastline with its various bays and peninsulas looks like a rough, jagged curve when viewed from hundreds of kilometers above the earth. When viewed by a person walking along its coves and points, this coastline again appears as a rough, jagged curve, and it retains this appearance even when considered from the perspective of an ant walking along individual grains of sand. This similar structure at many different scales is characteristic of fractals. In contrast, a beach ball on the same coastline looks like a point when seen from outer space, a sphere when viewed by a person walking along the shore, and a plane when considered by an ant on its surface. The substantially different appearance when viewed at different scales is more characteristic of non-fractal Euclidean structures.

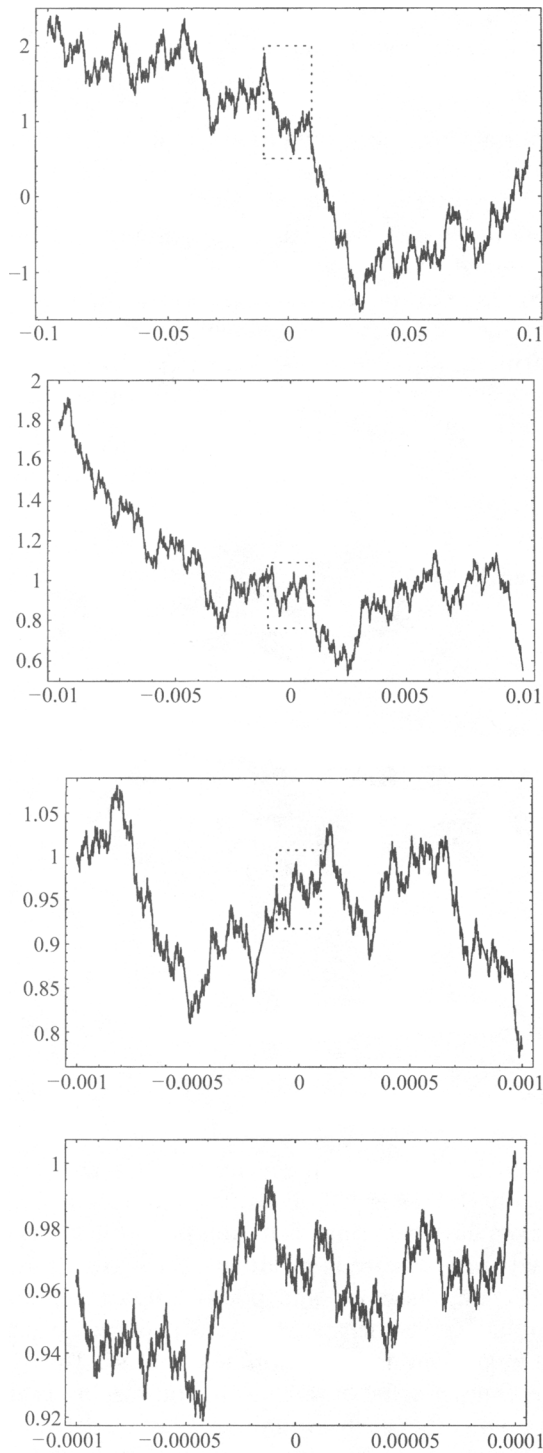
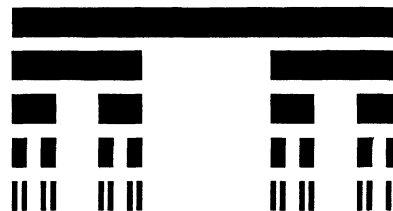


Figure 1.2 A bandlimited fractal Weierstrass function with dimension parameter $D = 1.5$, which has been shown to be an upper bound for the fractal dimension of the curve. As we zoom in on the curve, top to bottom with dashed lines indicating the magnified region, its general appearance does not change even though it does not possess strict self-similarity. This is considered to be self-similar in a statistical sense. [© 1999 Jaggard and Jaggard.]

Self-similarity may occur in either a statistical or an exact sense. In the former case, seen in the curve in Fig. 1.2, zooming in on one portion of the set reveals a subset that has the same general appearance as the whole set, with similar roughness and irregularity, without being an exact copy of the whole set. Exact self-similarity is seen in the stylized fractal pictured in Fig. 1.3. In this case, zooming in on a subset of the whole reveals a scaled replica of the entire set.

Figure 1.3 A triadic Cantor bar at stages of growth $S = 0, 1, 2, 3, 4$ (top to bottom), which has dimension $D_s = \ln 2/\ln 3 \approx 0.631$. This structure is strictly self-similar for discrete variations in magnification as each stage of growth contains two scaled copies of the set at the previous stage of growth.



Whether a fractal set has statistical or exact self-similarity, its similar appearance on all scales suggests that the set might be best constructed through recursive or iterative means. This stands in contrast to Euclidean structures, which may be more easily defined using formulae. We will also see that fractals may often be described with a non-integral dimension, in contrast to the integral dimension n assigned to Euclidean space \mathbb{R}^n . We summarize these and other qualitative differences between fractal and Euclidean geometry in Table 1.1.

TABLE 1.1 Heuristic Summary of Fractal and Traditional or Euclidean Geometrical Attributes. (Table after [1].)

Fractal Geometry	Euclidean Geometry
Often defined by iterative rule	Often defined by formula
Structure on many scales	Structure on one or few scales
Dilation symmetry (self-similarity)	No self-similarity
Fractional dimension possible	Integer dimension
Long-range correlation	Variable correlation
Described as ramified, variegated, spiky	Described as regular
Rough on most scales	Smooth on most scales

1.2.1.2 Bandlimited Fractals and Prefractals

While mathematically defined fractals exhibit an infinite range of scales, physical objects modeled by fractals, such as coastlines, trees, or naturally formed aggregates, cannot. Thus, as we try to model physical phenomena it is also useful to consider structures which display fractal characteristics over multiple scales but not the infinity of scales associated with fractals. In the case of statistical fractals, such structures are termed *bandlimited fractals*. These are constructed using the same methods as for true statistical fractals, but terminating construction when the additional structure to be added is smaller than a specified size, with the initiator providing the upper bound for the structure scales. For strictly self-similar fractals, the analogous concept is that of *prefractals*, which may be constructed by halting the fractal growth process after a finite number of steps. Bandlimited fractals and prefractals display self-similarity over a limited range of scales, looking like Euclidean space at sufficiently small scales.

While in a strict sense these are not fractals, we shall use the term *fractal* to describe fractals, bandlimited fractals, and prefractals.

1.2.1.3 Bandlimited Weierstrass Function

The fractal curve in Fig. 1.2 is the graph of a bandlimited Weierstrass function, which one might use to model the self-similar coastline described above. We will consider the definition of this function below, but at present we observe that the wild variations of this function allow it to somehow cover more of the plane than a smooth curve. Each of the bottom three plots in Fig. 1.2 is an enlarged picture of the middle one-tenth of the plot above it. While the shape of the graph is different with each enlargement, the function displays the same irregularity and roughness and thus a general self-similarity.

1.2.1.4 Triadic Cantor Set

The first fractal construction we will detail is the triadic Cantor set, one of the classic examples of a fractal set. As we broaden our ability to describe fractal sets, we will consider generalizations of this set that make use of our expanded means of characterizing fractals. The triadic Cantor set is formed by starting with the interval $[0, 1]$, the *initiator* of the fractal, and iteratively applying an operation which excises the middle third of each remaining closed interval, the *generator* of the fractal. In general, the initiator of an exact fractal is some structure taken as a starting point, and the generator is some operation—excision, addition, or replacement—which allows iterative modification of the initiator through repeated rescaling and application. Figure 1.3 shows stages of growth (= number of applications of the excising operation) $S = 0, 1, 2, 3$, and 4 of the triadic Cantor set.

Alternatively, we may construct the triadic Cantor bar by defining two functions $c_1: [0, 1] \rightarrow [0, 1/3]$ and $c_2: [0, 1] \rightarrow [2/3, 1]$ by

$$c_1(x) = \frac{x}{3} \quad (1.1)$$

$$c_2(x) = \frac{x + 2}{3} \quad (1.2)$$

These map the interval onto two disjoint subsets of itself, each shrinking the interval by a scaling factor $\gamma = 1/3$. In this method of construction, the Cantor bar at stage of growth $S + 1$ is formed by applying c_1 and c_2 to the Cantor bar at stage of growth S and taking the union of the two images, so that denoting by C_S the bar at stage of growth S , we have

$$C_{S+1} = c_1(C_S) \cup c_2(C_S) \quad (1.3)$$

with $C_0 = [0, 1]$. The triadic Cantor set C is the limit of this process as $S \rightarrow \infty$ and is seen to be the subset of $[0, 1]$ invariant under this mapping, that is,

$$C = c_1(C) \cup c_2(C) \quad (1.4)$$

Equation (1.4) highlights the self-similarity of C , which consists of two scaled copies of itself.

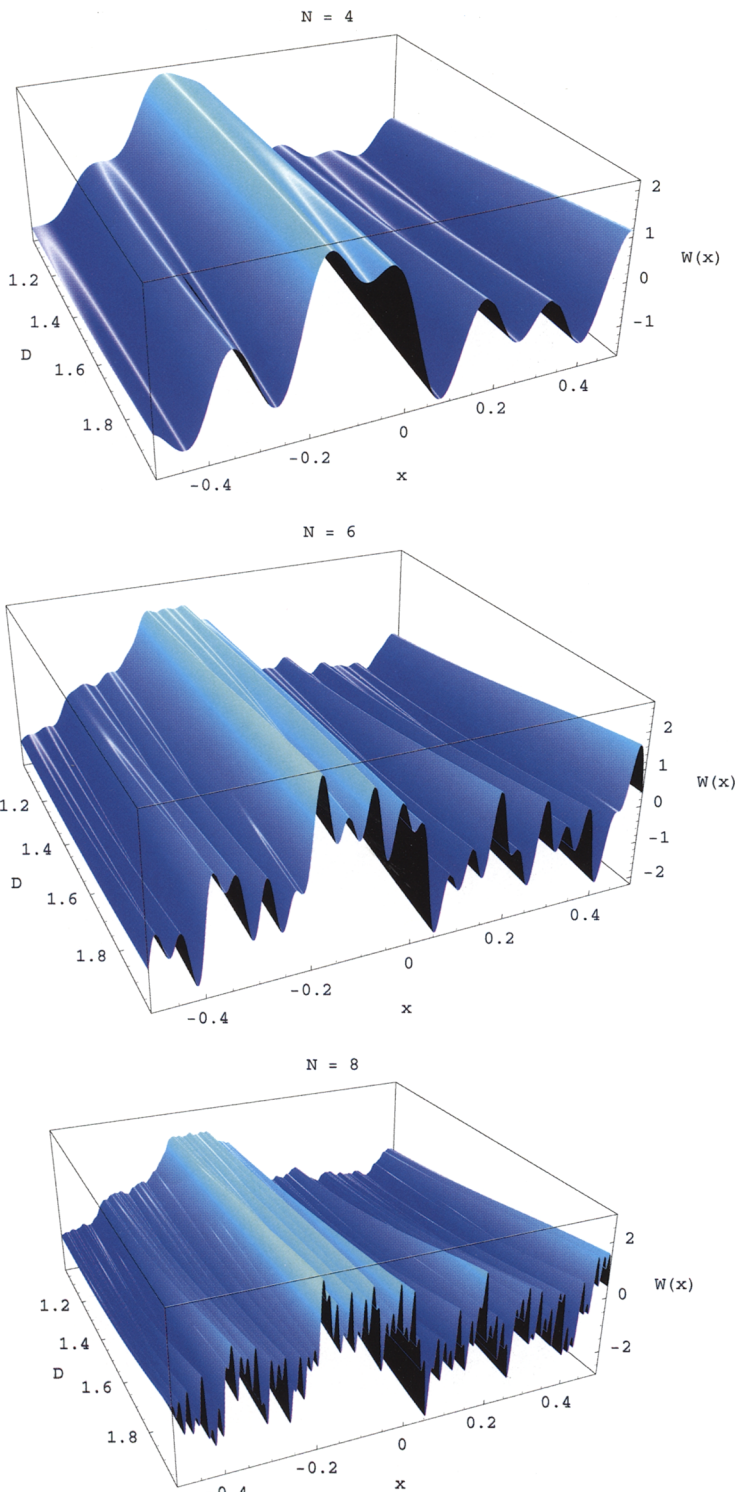


Figure 1.4 A bandlimited fractal Weierstrass function $W(x)$ as a function of coordinate x and dimension parameter $1 < D < 2$, $N = 4$ tones (top), $N = 6$ tones (middle), and $N = 12$ tones (bottom), with frequency parameter $b = 2e/3$. As $D \rightarrow 2$, the curve becomes area filling while as $D \rightarrow 1$ the curve becomes much smoother.

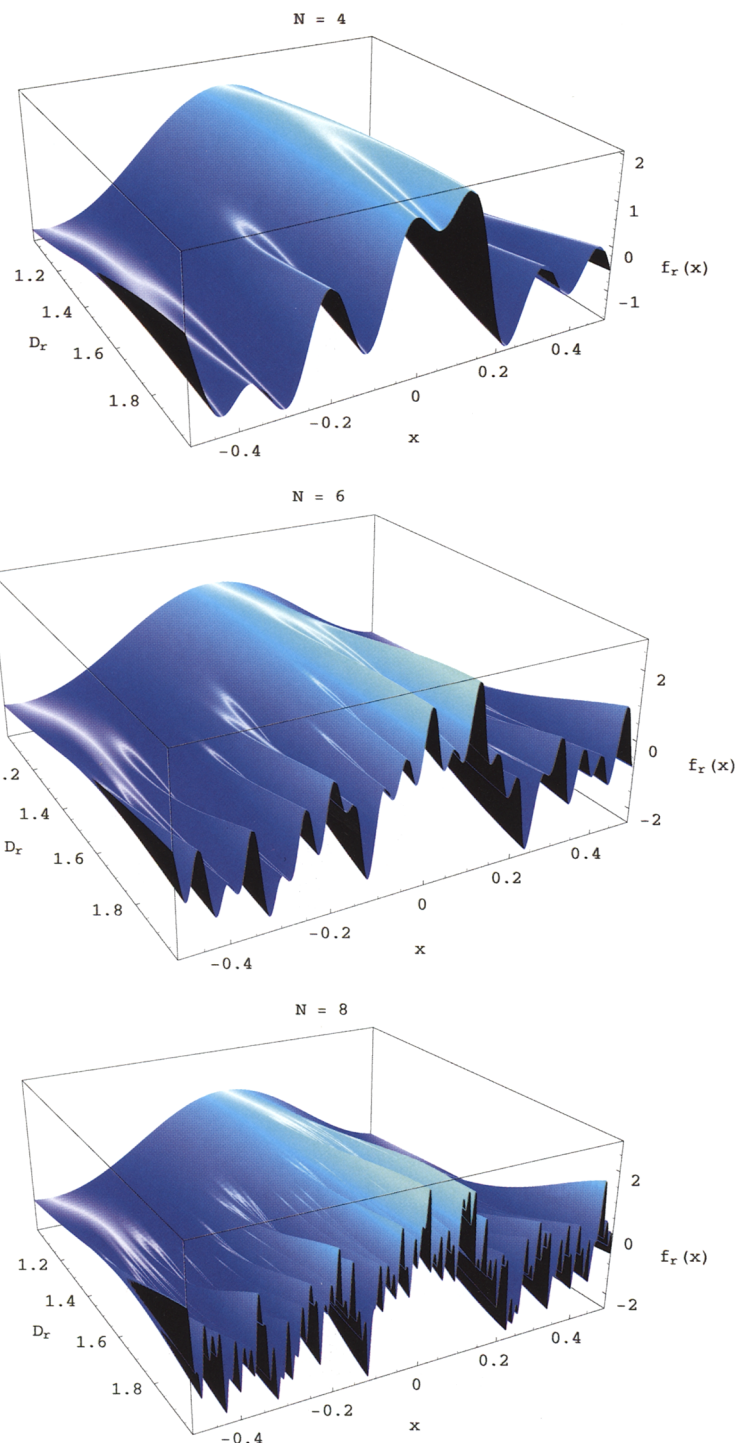


Figure 1.11 Plot of the fractal function $f_r(x)$ defined in relation (1.24) as a function of coordinate x for $1 < D_r < 2$ for $b = 2e/3$ and $N = 4$ tones (top), $N = 6$ tones (middle), and $N = 12$ tones (bottom). This self-similar function varies from smoothly undulating ($D_r \rightarrow 1$) to area-filling ($D_r \rightarrow 2$).

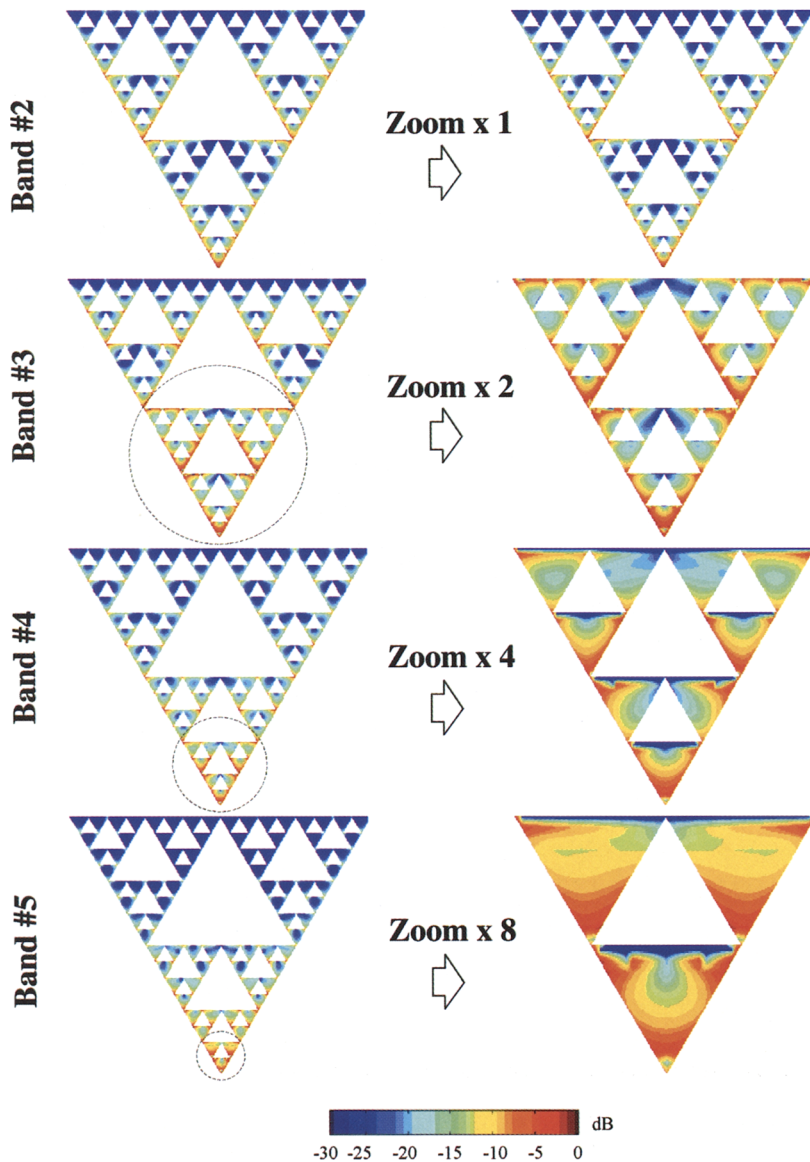
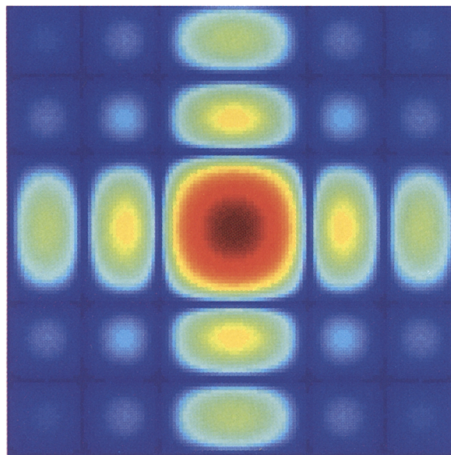


Figure 2.6 Current distribution on the Sierpinski antenna.

Cantor Square Diffraction



Stage 0



Stage 1



Stage 2

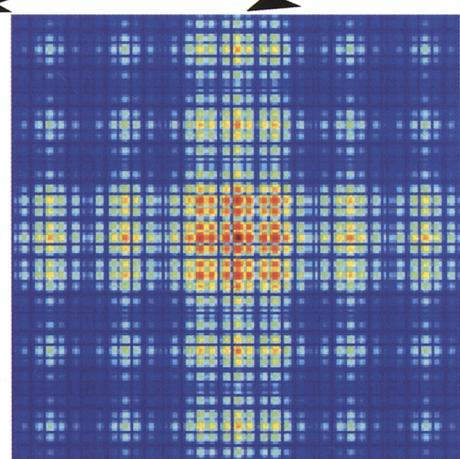
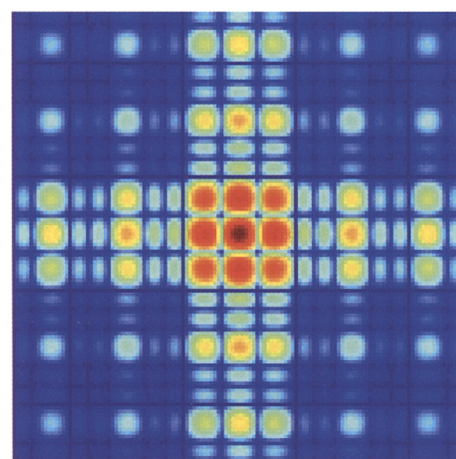


Figure 3.8 Aperture (top right) and diffracted field $|\Psi(x, y, z)/\Psi(0, 0, z)|$ in dB scale as a function of normalized spatial frequencies $f_x L$ and $f_y L$ for the three stages of growth $S = 0, 1, 2$ of a Cantor square. The axes are re-scaled by the factor $\gamma = 1/3$ for each successive stage of growth. The largest values are shown in dark red and the nulls in dark blue. (©1997 Jaggard and Jaggard [32].)

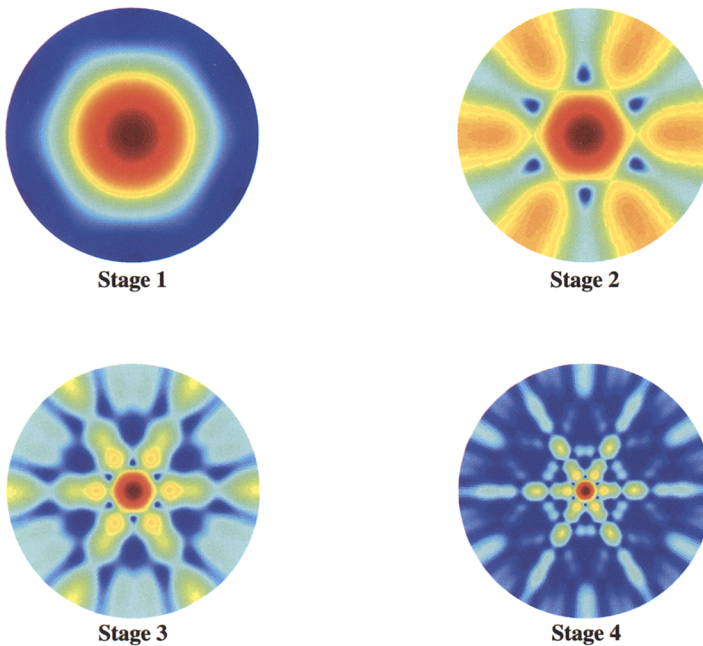


Figure 3.70 Color contour plots of the far-field radiation patterns produced by the four triangular arrays shown in Fig. 3.67. The angle ϕ varies azimuthally from 0° to 360° , and the angle θ varies radially from 0° to 90° .

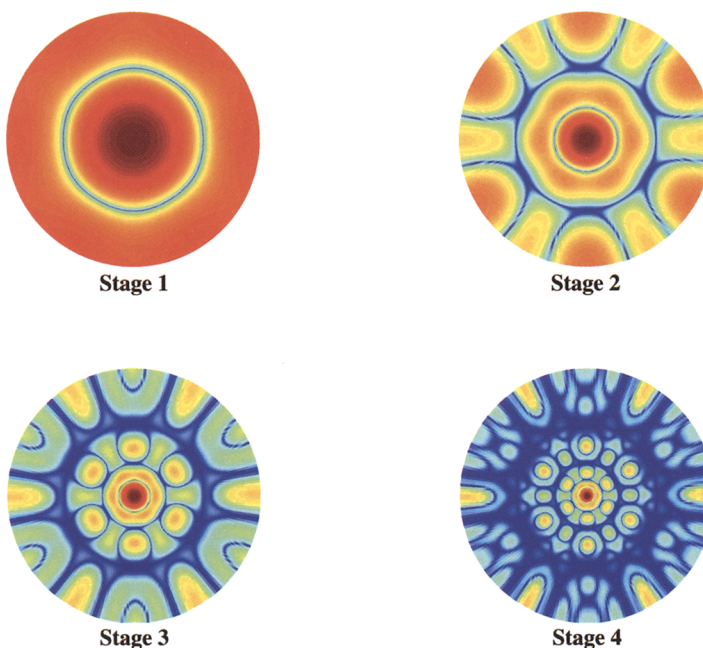


Figure 3.75 Color contour plots of the far-field radiation patterns produced by the four hexagonal arrays shown in Fig. 3.72 and Fig. 3.73. The angle ϕ varies azimuthally from 0° to 360° , and the angle θ varies radially from 0° to 90° .

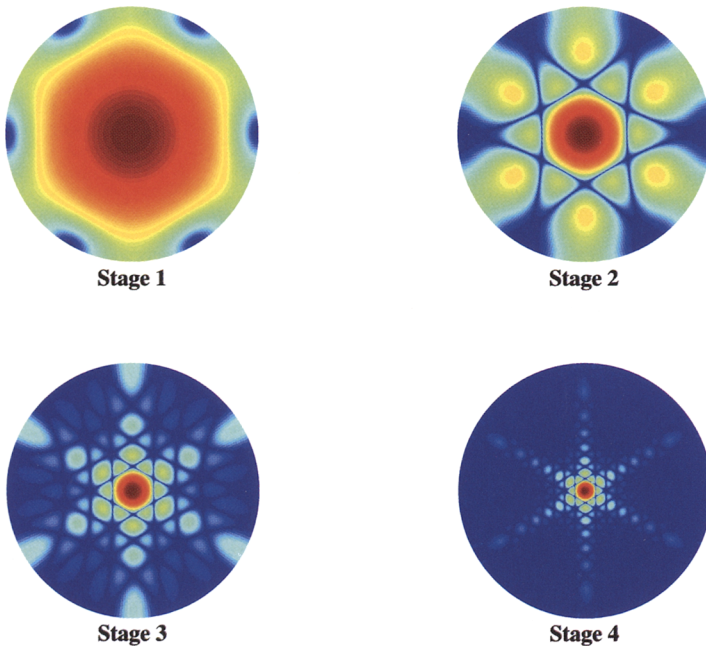


Figure 3.78 Color contour plots of the far-field radiation patterns produced by a series of four ($P = 1, 2, 3$ and 4) fully-populated hexagonal arrays generated with an expansion factor $\delta = 2$. The angle ϕ varies azimuthally from 0° to 360° , and the angle θ varies radially from 0° to 90° .

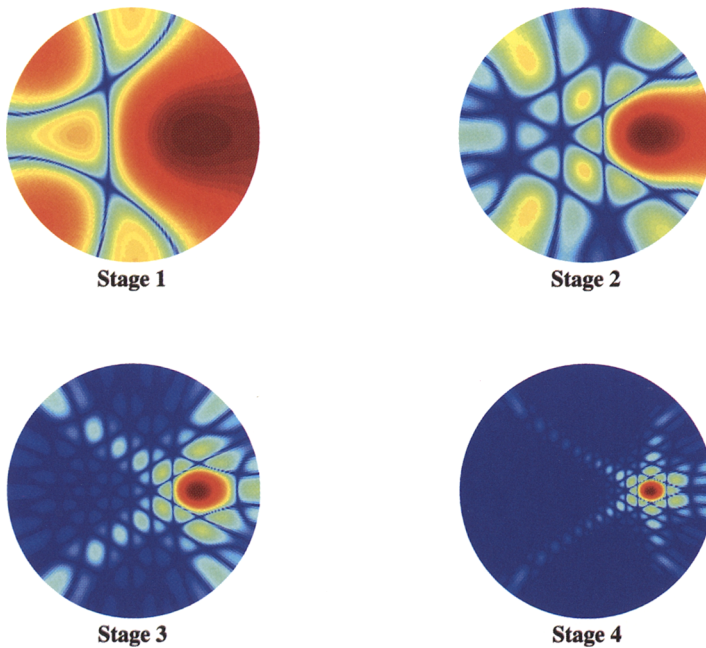


Figure 3.79 Color contour plots of the far-field radiation patterns produced by a series of four ($P = 1, 2, 3$ and 4) fully-populated hexagonal arrays generated with an expansion factor $\delta = 2$. In this case, the phasing of the generating subarray was chosen such that the maximum radiation intensity would occur at $\theta_0 = 45^\circ$ and $\phi_0 = 90^\circ$.

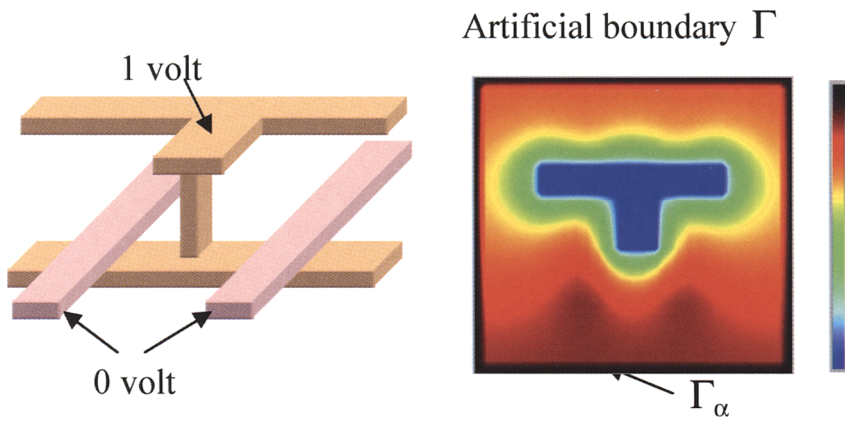


Figure 15.4 Potential distribution across the cross section that is parallel to the ground plane and located at the level of the upper T-shape conductor of the via.

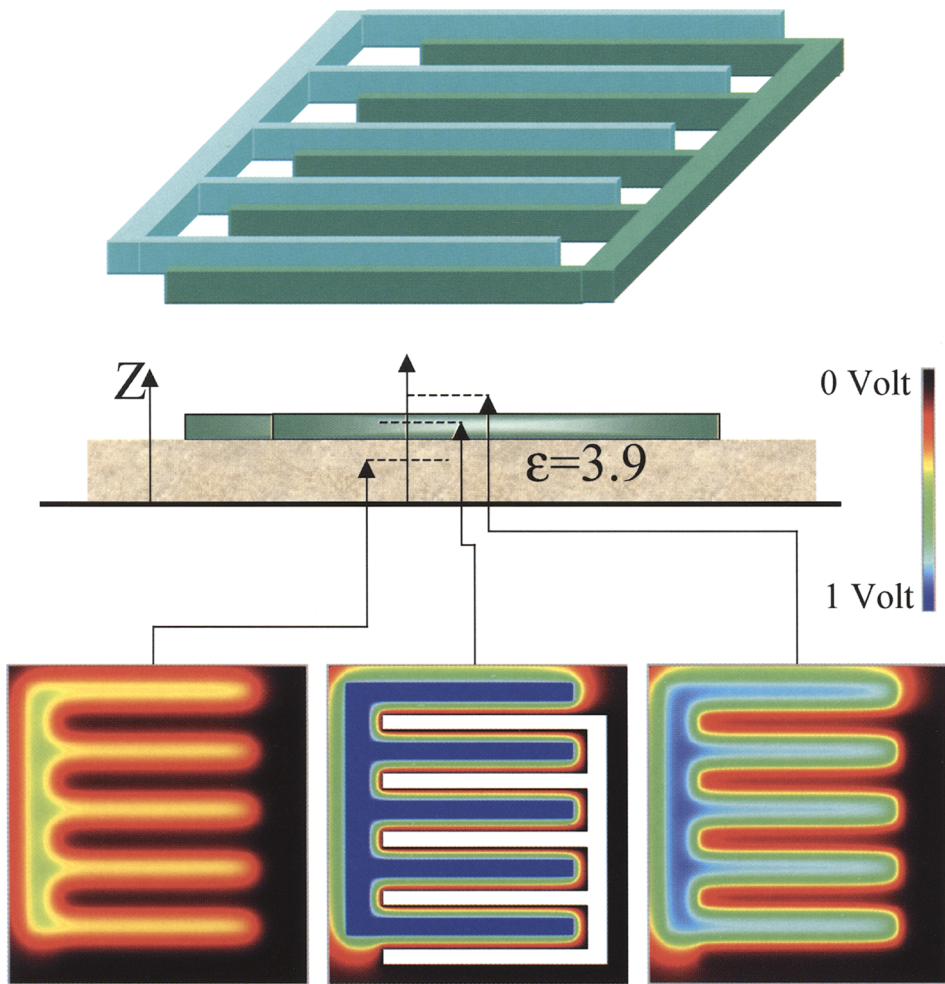


Figure 15.14 Two-comb structure. Potential distributions across the cross sections that are parallel to the ground plane.

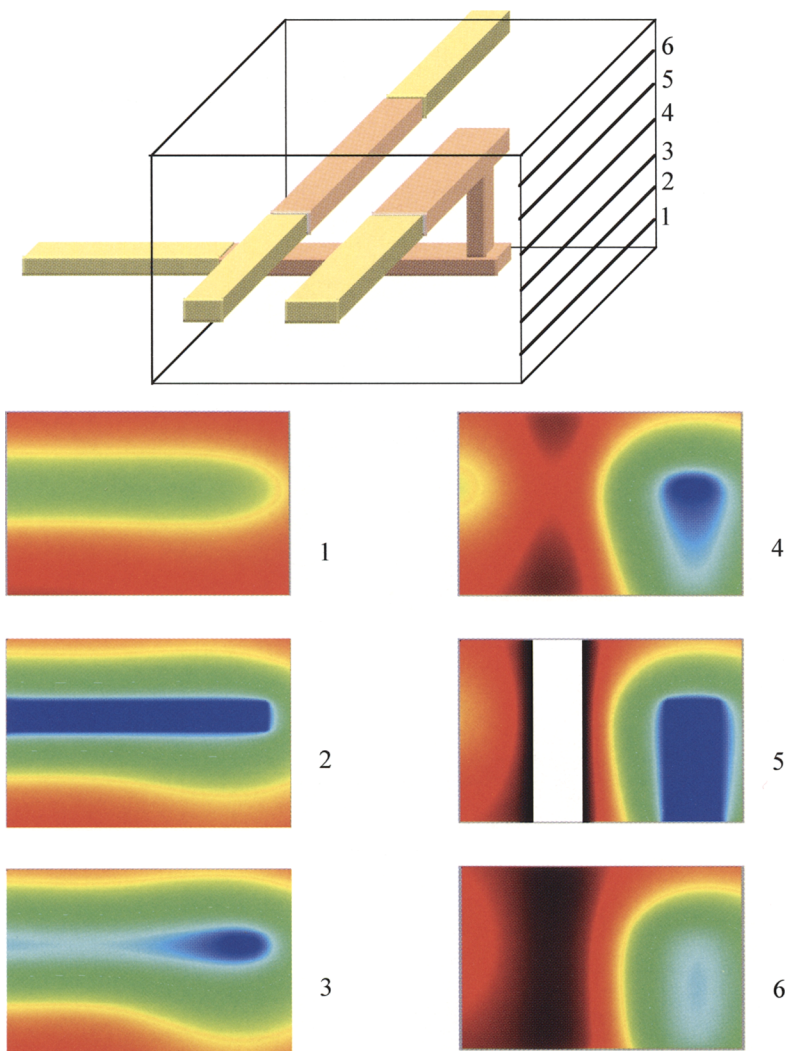


Figure 15.18 Potential distributions across the cross sections that are parallel to the $x-z$ plane in subdomain 3 at different levels with respect to the ground plane.

1.2.2 Fractal Dimension

1.2.2.1 Motivation

Having seen two examples of fractal sets, we observe that fractals often seem to fill different amounts of space than objects described by Euclidean geometry. A fractal curve in the plane, like that in Fig. 1.2, with its wiggles on all scales, is able to cover more of the plane than a smooth curve, but still does not fill the entire plane. The limit of the Cantor set in Fig 1.3 contains uncountably many points, but contains no intervals and so seems to fill qualitatively less space than the line. Finally, because of the infinite range of scales in a fractal, we can never consider a small enough region that the fractal looks like an n -dimensional Euclidean object. These considerations suggest that fractals might be viewed as having dimensions different than those of traditional geometric objects, and cause us to revisit the concept of dimension.

The following argument may be made to extend the notion of dimension from Euclidean objects to structures that we would like to be of non-integral dimension. If we wish to measure the length of the unit interval $[0, 1]$, we may count the number of intervals of length δ needed to cover the interval. Using our standard ideas about length, we need

$$N_{[0,1]}(\delta) = \left(\frac{1}{\delta}\right)^1 \quad (1.5)$$

such intervals to cover $[0, 1]$. To measure longer or shorter intervals, we may multiply $N_{[0,1]}$ by an appropriate constant (the length of the interval), but the δ^{-1} dependence will remain. Similarly, if we wish to measure the area of the unit square $[0, 1] \times [0, 1]$ we may count the number of squares of side δ needed to cover it. This is easily seen to be

$$N_{[0,1] \times [0,1]}(\delta) = \left(\frac{1}{\delta}\right)^2 \quad (1.6)$$

If we measure larger or smaller squares, the result will be the same up to a constant factor, in particular retaining the δ^{-2} dependence of $N_{[0,1] \times [0,1]}$. In general, if we wish to measure the size of the n -dimensional unit cube $[0, 1]^n$, we may cover it by

$$N_{[0,1]^n}(\delta) = \left(\frac{1}{\delta}\right)^n \quad (1.7)$$

n -cubes of side δ . The number of n -cubes of side δ needed to cover a general n -cube is proportional to δ^{-n} .

1.2.2.2 Definition

This suggests that we may view the exponent in the δ dependence of $N_{[0,1]^n}(\delta)$ as the dimension of the set $[0, 1]^n$ being covered, and that dimension might be extended to fractal sets in this manner. We count the number $N_E(\delta)$ of sets needed to cover a fractal set $E \subset \mathbb{R}^n$ with n -cubes, or multiple copies of another n -dimensional set. If

$$N_E(\delta) = C\delta^{-D}, \quad (1.8)$$

we have

$$D = \frac{\ln C - \ln N_E(\delta)}{\ln \delta} \quad (1.9)$$

For bounded fractal sets and sufficiently large δ , N_E has no δ dependence. Additionally, our intuition suggests that it is the *local* structure of fractals which differentiates them from Euclidean space. In this spirit we consider small δ , taking the limit of (1.9) as $\delta \rightarrow 0$. The $\ln C$ term then becomes insignificant, and we may define the *disk covering dimension*

$$D_d = \lim_{\delta \rightarrow 0} \frac{\ln N_E(\delta)}{-\ln \delta} \quad (1.10)$$

Just as covering a square with lines or a cube with squares is of minimal utility in this discussion, so is covering a fractal set E by sets of dimension less than that of E . To avoid this, we use n -dimensional sets to cover a set $E \subset \mathbb{R}^n$.

Consider a strictly self-similar fractal E which contains N copies of itself, each scaled by a factor γ . The S^{th} stage of growth defines a cover of E by N^S sets of size $C\gamma^S$, where C is a constant depending on the size of the initiator (0^{th} stage). Forming an expression similar to Eq. (10), we have

$$\frac{\ln N^S}{-\ln C\gamma^S} = \frac{S \ln N}{-(\ln C + S \ln \gamma)} \quad (1.11)$$

As $S \rightarrow \infty$ and the size of the covering sets $C\gamma^S \rightarrow 0$, the $\ln C$ term vanishes. This leads to the *similarity dimension* for strictly self-similar sets, defined as

$$D_s = \frac{\ln N}{-\ln \gamma} \quad (1.12)$$

for sets consisting of N non-overlapping copies of the whole, each scaled by a factor γ .

The triadic Cantor bar in Fig. 1.3 consists of two copies of itself scaled by $1/3$. Thus, it has similarity dimension $\ln 2/\ln 3 \approx 0.631$. This agrees with our expectations for the dimension of this set, since it seems to be qualitatively more than a (zero-dimensional) point without completely filling the (one-dimensional) interval $[0, 1]$, and in fact not filling *any* interval $[a, b]$.

1.2.2.3 Extensions

The computation of the disk-covering dimension is suitable for adaptation to automated systems. These might use a fixed grid with cells of size δ , counting the number of cells intersecting the set E in question to find $N_E(\delta)$. This approach has applications to the computation of dimension for naturally occurring aggregates, electrical discharges, and digitized images. When implemented with a fixed grid, this is usually referred to as the *box-counting dimension*.

There are a number of other fractal dimensions used in describing fractal sets. Further discussion can be found in [36–37], [41], with a more formal approach given in [34].

Bandlimited fractals and prefractions have integral dimension, for at sufficiently

small scales they look like Euclidean objects. However, we will still refer to the “fractal dimension” of these types of sets. For bandlimited fractals, we will often take as the dimension the value of D_d suggested by the disk-covering procedure using disks whose size is within the range of scales present in the structure of the prefractal. In the case of exact prefractals, we define the dimension as that of the fractal for which the prefractal is some finite stage of growth. The fractal dimension of these structures is useful in investigating their properties on scales at which they are indistinguishable from a true fractal, for example electromagnetic interrogation of a prefractal when the frequencies used are too low to resolve the omitted fine structure.

1.2.3 Fractals and Their Construction

Since one common characteristic of fractals is self-similarity, we look to the construction of self-similar sets as one means of obtaining additional examples of fractals. This will provide a few illustrations of the concept and computation of fractal dimension. We first give the construction of the Weierstrass function and then give that of the Sierpiński gasket, a strictly self-similar fractal in the plane \mathbb{R}^2 . We conclude with a generalization of the triadic Cantor bar.

1.2.3.1 Bandlimited Weierstrass Function

We now construct the bandlimited Weierstrass function $W(x)$ shown in Fig. 1.2. The graph of this function is not strictly self-similar, as the Cantor set is, but does display self-similarity in the sense of having a similar appearance at different scales. This self-similarity is not surprising if we consider the definition of the function

$$W(x) = C \sum_{n=N_1}^{N_2} b^{n(D-2)} \cos(2\pi s b^n x + \theta_n) \quad (1.13)$$

where D is the dimension parameter, $s b^{N_1}$ and $s b^{N_2}$ ($b > 1$) are the lowest and highest spatial frequencies, the θ_n are random phases in $[0, 2\pi]$, and C is an appropriate constant [1]. The plots in Fig. 1.2 are for $N_1 = 1$, $N_2 = 40$, $b = 2e/3$, $s = 1$, and $D = 1.5$. As N_2 increases, $W(x)$ contains increasingly fine structure due to the addition of high-frequency sinusoids. For a finite number of tones $N = N_2 - N_1 + 1$, $W(x)$ is a bandlimited fractal, displaying fractal characteristics on scales between $(s b^{N_2})^{-1}$ and $(s b^{N_1})^{-1}$.

As $D \rightarrow 1$ the lowest frequency sinusoid in the summation defining $W(x)$ becomes dominant and the function approaches a smoothly undulating curve. As $D \rightarrow 2$, the sinusoids in the summation have almost equal contributions and the curve becomes very jagged and starts to fill up the plane. This “dimension parameter” thus behaves much as we would expect a measure of fractal dimension to behave, and has in fact been shown to be equal to the box counting dimension in certain cases [41]. Functionally defined fractals such as $W(x)$ often have similar dimension parameters which control the apparent roughness of the function but which have not necessarily been proven to be equal to any of the measures of fractal dimension for the particular function. A generalization of the Weierstrass function is used to form the fractal mountains in Fig. 1.1.

In Fig. 1.4 (see full-color insert) is shown the Weierstrass function in relation (1.13) as a function of the continuous variable D and coordinate x for number of tones $N = 4$ and 12.

1.2.3.2 Sierpiński Gasket

The Sierpiński gasket is shown in Fig. 1.5 for the first six stages of growth. We construct this fractal by taking a filled equilateral triangle (top left) as the initiator and an operation which excises an inverted equilateral triangle which is the initiator inverted and scaled by one-half as the generator (top right). Application of the generator leaves three smaller filled triangles, to which we may apply a scaled copy of the generator. We iterate this process to obtain higher stages of growth.

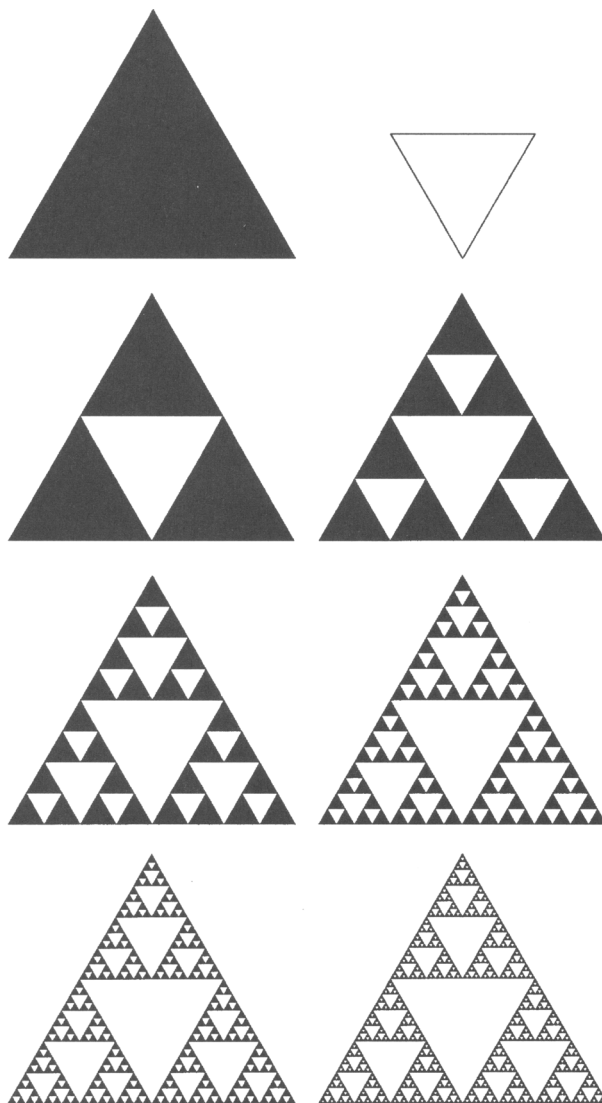


Figure 1.5 The construction of the Sierpiński gasket, which has dimension $D_s = \ln 3/\ln 2 \approx 1.58496$, with initiator (top left) and generator (top right) and stage of growth $S = 1, 2, 3, 4, 5, 6$. This dimension corresponds to our intuitive feeling for the dimension of the set, which contains straight lines, but is unable to “fill up” the plane as $S \rightarrow \infty$.

From the perspective of mappings from $\mathbb{R}^2 \rightarrow \mathbb{R}^2$, we may define

$$s_1(x, y) = \left(\frac{x}{2}, \frac{y}{2} \right) \quad (1.14)$$

$$s_2(x, y) = \left(\frac{x+1}{2}, \frac{y}{2} \right) \quad (1.15)$$

$$s_3(x, y) = \left(\frac{2x+1}{4}, \frac{2y+\sqrt{3}}{4} \right) \quad (1.16)$$

If the initiator (zeroth stage) of the Sierpiński gasket has side length 1 with its lower left vertex at the origin and the bottom edge coincident with the x -axis, the maps s_1 , s_2 , and s_3 take this triangle to the lower left, lower right, and top triangles seen in the first stage of construction. As with the triadic Cantor set, the $(S+1)^{\text{st}}$ stage of growth is the union of the images of the S^{th} stage of growth under the (in this case three) defining maps. The Sierpiński gasket is the limit of this process as $S \rightarrow \infty$ and is invariant under this operation.

1.2.3.3 Polyadic Cantor Bars—Minimal Lacunarity

The construction of the Cantor bar discussed above is easily generalized to give different values of D_s . The first generalization is a variation in γ , so that an amount other than the middle third is excised from each interval. We change the generator to be the operation which excises the middle $1 - 2\gamma$, $\gamma \in (0, \frac{1}{2})$, of each interval. Equivalently, these Cantor bars contain two copies of the whole set, each scaled by γ and thus have similarity dimension $D_s = \ln 2 / \ln(1/\gamma)$. With the appropriate choice of γ , we may construct a “single-gap” Cantor bar with any value of D_s between 0 and 1 as shown in Fig. 1.6 for $D_s = 1/2$ and $3/4$.

As D_s is a function of both γ and the number N of scaled copies of the whole, we might also try changing N . We extend the Cantor bar construction using a generator that excises $n_{\text{gaps}} > 1$ intervals. Equivalently we may define $N = n_{\text{gaps}} + 1 > 2$ maps $\{c_i\}_{i=1}^N$ of the unit interval into subintervals, analogous to the maps c_1 and c_2 that gave

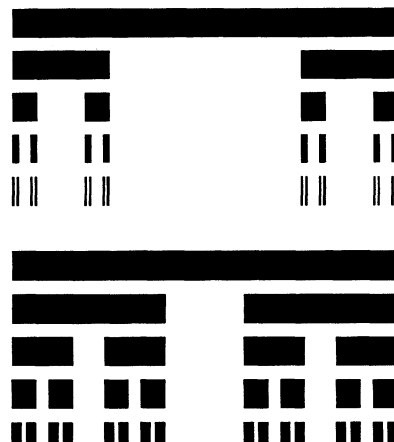


Figure 1.6 Stages of growth $S = 0, 1, 2, 3, 4$ for single-gap Cantor bars with $D_s = 1/2$ (top) and $3/4$ (bottom).

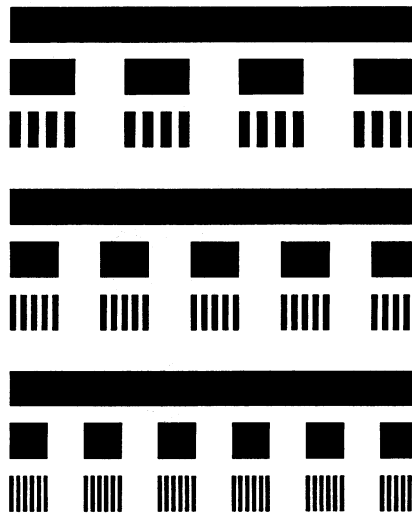


Figure 1.7 Stages of growth $S = 0, 1, 2$ for three-, four-, and five-gap Cantor bars (top to bottom) with the scaled copies of the set uniformly distributed within the unit interval. In each case $D_s = 3/4$.

the triadic Cantor bar. We will restrict our attention to Cantor bars in which the sizes of the intervals remaining after each excising operation (i.e., the scaling ratios of the N maps from the interval to subintervals) are the same value γ . In cases where these values are different ($= \{\gamma_i\}_{i=1}^N$) the fractal dimension is the value of D_s which satisfies $\sum_{i=1}^N \gamma_i^{D_s} = 1$ [37]. For the moment we also require the subintervals to which the interval is mapped to be uniformly spaced throughout the interval. Examples of such Cantor bars are pictured in Fig. 1.7, with $n_{gaps} = 3, 4$, and 5 (top to bottom). We will examine some of the effects of relaxing the uniform spacing condition below.

1.2.4 Lacunarity

1.2.4.1 Concept

Fractal dimension is the primary descriptor of fractal sets and structures. However, just as knowing the Euclidean dimension of an object does not determine the object (e.g., a curve of dimension one may be a straight line or a smoothly varying curve such as a sinusoid), knowing the fractal dimension D_s does not uniquely determine the fractal set under consideration. Figure 1.8 shows two square Sierpiński carpets at the second stage of growth, each of which consists of $N = 40$ copies of the whole set, with each copy scaled by $\gamma = 1/7$. Both have similarity dimension $D_s = \ln 40/\ln 7$, but they appear very different due to the different arrangements of the scaled copies within the set. We might also think of these two carpets as in some sense covering the same amount of space but doing so in different ways. Because dimension does not completely describe a fractal set, we look for other fractal descriptors to provide additional information about fractal structures.

Mandelbrot introduced lacunarity [78], from the Latin *lacuna* (gap), to describe the differences between the carpets in Fig. 1.8. Fractals with large gaps have large lacunarity, while fractals with small gaps have small lacunarity. We may also think of highly lacunar fractals as those which are very inhomogeneous and far from being translationally invariant, while fractals of low lacunarity are more homogeneous and

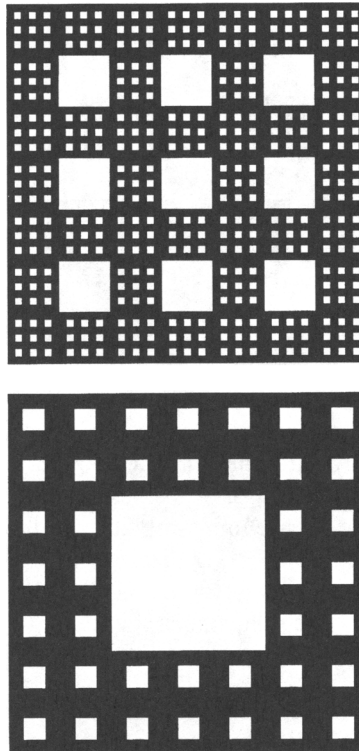


Figure 1.8 Two Sierpiński carpets of dimension $D_s = \ln 40 / \ln 7$. Their different appearances suggest the need for additional fractal descriptors. The same fractal dimension for these sets means there is the same amount of black ink used in printing them, while the different lacunarities indicate that the ink is distributed differently. [Figure after [78].]

approach translational invariance. While the fractal dimension gives a measure of how much space is filled by a set, lacunarity gives an idea of the way in which it is filled or the texture of the set. The Sierpiński carpet on the top of Fig. 1.8, in which the black area is more homogeneously distributed throughout the square, has low lacunarity while the one on the bottom, with its large gap in the center and highly inhomogeneous appearance, has high lacunarity.

1.2.4.2 Examples—Polyadic Cantor Bars with Variable Lacunarity

Having seen one pair of fractals with differing lacunarity, we consider other examples to illustrate this measure of texture. Following the example of the Sierpiński carpets in Fig. 1.8, we take a previously defined self-similar fractal and rearrange the subcopies of the whole while continuing to keep them non-overlapping. One family of fractals we have seen which is immediately amenable to this generalization is the family of polyadic Cantor bars discussed in Section 1.2.3.3.

Because of physical considerations from the problem of reflection from a Cantor superlattice in Section 1.4, we continue to impose some restrictions on the positioning of the subintervals within the original interval. The Cantor bars we consider must be symmetric about their midpoint, that is, for a Cantor bar C constructed in $[0, L]$, $x \in C \Leftrightarrow L - x \in C$. Additionally, we require the outer $\lfloor (n_{\text{gaps}} - 1)/2 \rfloor$ gaps between subintervals be of equal size εL . For n_{gaps} odd or even, we have a central gap or bar,

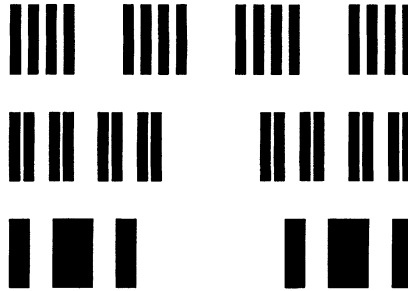


Figure 1.9 The second stage of growth for three-gap Cantor bars of low, medium, and high (top to bottom) lacunarity. The corresponding values of ε are $\varepsilon_{max} \approx 0.123$, $\varepsilon_{max}/2 \approx 0.0617$, and 0. Each bar has dimension $D_s = 3/4$.

respectively, with the midpoint symmetry forcing the two gaps on either side of the central bar to be of equal size in the n_{gaps} even case. All gaps other than the centermost gap(s) are of size εL . The value of ε determines the size of the centermost gap(s).

Three-gap Cantor bars at the second stage of growth are shown in Fig. 1.9 for three different values of ε . We see that for $\varepsilon = \varepsilon_{max} = (1 - N\gamma)/n_{gaps}$ (top), the subcopies of the set are uniformly distributed and the set appears fairly homogeneous and of low lacunarity. As ε decreases to 0 (middle and bottom), the central gap becomes larger and the set appears more “gappy” and inhomogeneous. As discussed below, over this range lacunarity appears to be a monotonically decreasing function of ε for polyadic Cantor bars, and we use ε to characterize the lacunarity of this family of Cantor bars.

1.2.4.3 Definition

As one potential measure of lacunarity, we adapt the *gliding box method* proposed by Allain and Cloitre [79]. The formulation given here is for linear fractals such as Cantor sets, but generalizations would allow measurement of the lacunarity of the planar carpets in Fig. 1.8. In this approach, we overlay a box of radius R on the set in question, and let $Q(M, R)$ be the probability that it covers mass M . If we define the q th moment of Q by

$$Z_Q^{(q)} = \sum_M M^q Q(M, R) \quad (1.17)$$

then a measure of lacunarity may be defined as

$$\Lambda(R) = \frac{Z_Q^{(2)}(R)}{[Z_Q^{(1)}(R)]^2} \quad (1.18)$$

If we let M_R be the mass covered by a box of radius R and denote by $\langle \cdot \rangle$ average value, we see that

$$\Lambda(R) = \frac{\langle M_R^2 \rangle}{\langle M_R \rangle^2} \quad (1.19)$$

For a generalized Cantor bar $C_{(\varepsilon)}$ with outer gap width ε in which we are interested, we may define

$$K_\varepsilon^R(\tau) = \int_{\tau-R}^{\tau+R} \chi_{C_{(\varepsilon)}}(x) dx = \int_{-\infty}^{\infty} \chi_{C_{(\varepsilon)}}(x) h_R(x - \tau) dx \quad (1.20)$$

where

$$\chi_E(x) = \begin{cases} 1, & x \in E \\ 0, & x \notin E \end{cases} \quad (1.21)$$

is the characteristic function of the set E and we have defined the window function $h_R(x) = \chi_{[-R,R]}(x)$ to give K_ε^R the form of a cross-correlation. Analogously to (1.19) we integrate K_ε^R and $(K_\varepsilon^R)^2$ over all allowable values of τ , obtaining the expression

$$\Lambda_\varepsilon(R) = \frac{\int_{\tau_{min}}^{\tau_{max}} K_\varepsilon^R(\tau)^2 d\tau}{\left[\int_{\tau_{min}}^{\tau_{max}} K_\varepsilon^R(\tau) d\tau \right]^2} \quad (1.22)$$

for lacunarity in the setting of this family of Cantor bars. For a Cantor set in $[0, L]$, we take $[\tau_{min}, \tau_{max}]$ to be $[R, L - R]$ so that the support of the window function h_R is always contained in $[0, L]$. This expression for lacunarity is dependent upon the window radius R , but we may define $\tilde{R} = (\gamma + \varepsilon_{max})L/2$ and

$$\tilde{\Lambda}(\varepsilon) = \Lambda_\varepsilon(\tilde{R}) \quad (1.23)$$

As shown in [77], $\tilde{\Lambda}$ appears to be monotonic with ε over $[0, \varepsilon_{max}]$, suggesting that ε is a reasonable descriptor of lacunarity for this family of Cantor sets. Because ε has useful interpretations in fractal electrodynamics problems, we will use it as our primary means of quantifying lacunarity.

1.2.5 Fractals and Waves

We have seen that the common characteristics of fractals include self-similarity and structure at many different scales. These traits suggest that fractals may fall “in between” Euclidean spaces and possess non-integer dimension. Using the many-scale structure of fractals, we are able to define reasonable measures of dimension and texture for fractals.

Our discussion of fractals has made use of variable length yardsticks, both in describing the scales on which a fractal has structure and in computing a fractal’s dimension. If we are investigating fractal electrodynamics problems, we might look for *electromagnetic yardsticks* of variable size. The wavelength and pulse width of interrogating signals give us variable scale tools with which to investigate fractal structures in the frequency-domain and time-domain, respectively. We now turn our attention to the use of these tools in the problems of wave scattering from fractal surfaces and superlattices.

1.3 SCATTERING FROM FRACTAL SURFACES

For decades, scattering of optical, electromagnetic and acoustical waves from rough surfaces has been a key theoretical and experimental problem in science and engineering. Often the goal has been the remote characterization of microscopically

rough interfaces, sea surfaces, ocean bottoms, and rough terrain. Other applications include surface imaging, the classification or characterization of naturally occurring and manufactured objects, and non-destructive evaluation and testing. In these past studies, deterministic periodic functions, random functions or distributions, and random iterations have been used in the mathematical modeling of rough surfaces. Concepts developed in fractal electrodynamics have provided a useful tool to describe electromagnetic interactions with multiscale rough structures. Naturally occurring rough surfaces are often formed through repetitive actions of nature that yield bandlimited fractals, carefully balancing ordered and chaotic processes.

Here we examine the scattering of electromagnetic waves from rough surfaces first using the Kirchhoff or physical optics approximation and then using the exact transition matrix (T-matrix) approach or extended boundary condition method (EBCM). The approximate solution provides physical insight into the scattering, yields a simple relation between the scattering data and the fractal dimension, and in the appropriate limit, provides a touchstone for the subsequent numerical results. This approximate method involves a simplified scalar approach that does not take polarization into account. The T-matrix approach validates the approximate method in the regime of appropriately shallow and smooth corrugations for near-normal incidence illumination. The exact method also allows an investigation of the effect of increased roughness and an examination of the effect of polarization, both of which are inaccessible to most approximate techniques.

1.3.1 Problem Geometry

The geometry used here is given in Fig. 1.10 in which an incident plane wave illuminates a fractal surface patch of length $2L$ at an incident angle θ_i with respect to the surface normal of the reference ($z = 0$) plane. The incident and scattered wavenumbers are \mathbf{k}_i and \mathbf{k}_s , respectively, and have magnitude equal to the free space wavenumber k . In the smooth surface or low-frequency limit, the scattered field has a specular component whose mainlobe width is inversely proportional to both the patch size and the wavenumber of the illuminating wave. As the roughness of the

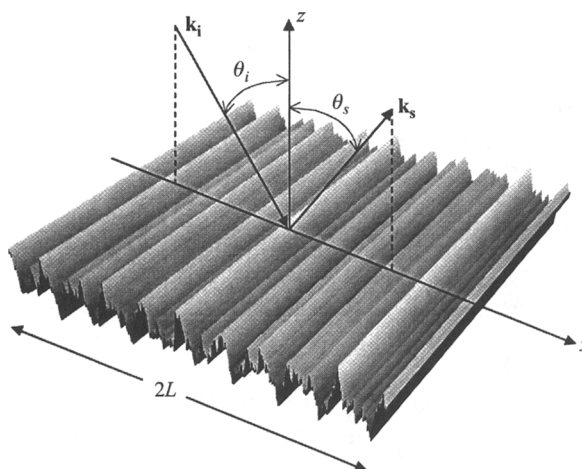


Figure 1.10 Geometry of rough surface scattering problem in which an incident plane wave illuminates a fractal surface patch of size $2L$ at an angle θ_i with respect to the reference plane ($z = 0$) normal. The scattering cross section is calculated for various scattering angles θ_s . The fractal function $f_r(x)$ defines the rough surface and \mathbf{k}_i and \mathbf{k}_s are the incident and scattered wavevectors, respectively. [© 1999 Jaggard and Jaggard.]

surface increases, or as the frequency increases, the specular component of reflection is reduced as nonspecular components play an increasingly dominant role. As a result, larger amounts of the scattered power are redistributed over an increasing number of directions due to diffraction.

The surface patch roughness for both the approximate and exact cases considered in this chapter is described by the one-dimensional bandlimited *fractal function* that is a mathematical relative to the bandlimited Weierstrass function developed for other problems in fractal electrodynamics [1], [18], [19], [80] and defined in (1.13). This fractal function is given by

$$f_r(x) = \sigma C \sum_{n=0}^{N-1} (D_r - 1)^n \sin(K_0 b^n x + \phi_n) \quad (1.24)$$

where $D_r \in (1, 2)$ is the *roughness fractal dimension*,¹ $K_0 = 2\pi/\Lambda_0$ is the fundamental spatial wavenumber of the surface, Λ_0 is the corresponding fundamental spatial frequency, $b > 1$ is the spatial frequency scaling parameter, ϕ_n are specified or random phases, and N is the number of tones or spatial frequencies describing the surface. The amplitude factor is given by

$$C = \sqrt{\frac{2D_r(2 - D_r)}{[1 - (D_r - 1)^{2N}]}} \quad (1.25)$$

and is chosen so that the function has a standard deviation or *rms* height σ . Note that $f_r(x) \approx (D_r - 1)f_r(bx)$ so that the function is discretely self-similar as the number of tones becomes sufficiently large. The *rms* slope of the surface given by (1.24) is found to be

$$\sigma_s = K_0 \sigma \sqrt{\frac{[1 - (D_r - 1)^2][1 - b^{2N}(D_r - 1)^{2N}]}{[1 - (D_r - 1)^{2N}][1 - b^2(D_r - 1)^2]}} \quad (1.26)$$

Plots of the fractal function (1.24) for $N = 4$ and 12 are shown in Fig. 1.11 (see full-color insert) as a function of continuous independent variable x and roughness fractal dimension D_r . As D_r increases the roughness increases due to the enhancement of the higher spatial frequencies in (1.24). Its value ranges from $D_r \rightarrow 1$ (smooth periodic curve) to $D_r \rightarrow 2$ (rough, area-filling curve). Likewise, as the number of tones N increase, small scale roughness becomes apparent for moderate and larger values of dimension, $D_r \geq 1.5$.

1.3.2 Approximate Scattering Solution

1.3.2.1 Formulation of Approximate Surface Scattering Solution

Under the Kirchhoff, physical optics, or undisturbed field approximation, the scattered field is given by an integration over the illuminated surface patch of the

¹From the plots it appears that D_r acts qualitatively as a fractal dimension and has the expected effect in the limiting cases $D_r \rightarrow 1$ and $D_r \rightarrow 2$. However, it has not been proven that D_r is equal to one of the common fractal dimensions.

incident field. The phase delay imprinted on the scattered field provides its fractal signature. The Kirchhoff approximation treats the rough surface as locally flat with the assumption that the wavelength of the incident wave is small compared to the radius of curvature of the surface corrugation. Incident angles close to normal incidence for the smooth surface will be used to avoid shadowing. The scattering results shown here satisfy all of these requirements. The geometry is shown in Fig. 1.10, and the analysis follows the formulation of Beckmann and Spizzichino [81].

The scattered field at the observation distance r from the origin is given by

$$\Psi_{sc}(\theta_i, \theta_s) = \frac{ikLe^{ikr}}{4\pi r} \iint_{S_{fractal}} [pf'_r(x') - q] e^{ik_x x' + ik_z f_r(x')} dx' dy' \quad (1.27)$$

with

$$\begin{aligned} p &= (1 - R) \sin(\theta_i) + (1 + R) \sin(\theta_s) \\ q &= (1 + R) \cos(\theta_s) - (1 - R) \cos(\theta_i) \\ k_x &= +k[\sin(\theta_i) - \sin(\theta_s)] \\ k_z &= -k[\cos(\theta_i) + \cos(\theta_s)] \end{aligned} \quad (1.28)$$

where R is the appropriate Fresnel reflection coefficient of the tangent plane at the point of interest and $f'_r(x)$ is the derivative with respect to its argument, and the integrals are evaluated over the illuminated patch $S_{fractal}$. We consider here the case of scattering from a perfectly conducting rough surface where the magnitude of the Fresnel reflection coefficient is unity.

Evaluating the integral in (1.27) we find that after integrating by parts and assuming that the patch size is much larger than a wavelength, the scattering cross section or scattering coefficient

$$\frac{d\sigma(\theta_i, \theta_s)}{d\theta_s} = \left| \frac{\Psi_{sc}(\theta_i, \theta_s)}{\Psi_{max}} \right|^2$$

is found to be [50]

$$\begin{aligned} \frac{d\sigma(\theta_i, \theta_s)}{d\theta_s} &= \left| \sec(\theta_i) \frac{1 + \cos(\theta_i + \theta_s)}{\cos(\theta_i) + \cos(\theta_s)} \right|^2 \times \\ &\quad \left| \sum_{m_0, m_1, \dots, m_{N-1} = -\infty}^{+\infty} e^{[i \sum_{n=0}^{N-1} m_n \phi_n]} \prod_{n=0}^{N-1} J_{m_n} [C(D_r - 1)^n k_z \sigma] \operatorname{sinc}[(m_n b^n K_0 + k_x) L / \pi] \right|^2 \end{aligned} \quad (1.29)$$

where Ψ_{max} is the specularly scattered field when the surface is smooth and we use the notation $\operatorname{sinc}(x) \equiv \sin(\pi x) / (\pi x)$.

It can be shown from (1.29) that the decrease in the specular scattering is proportional to the variance of the surface height as given by the relation

$$\left| \frac{\Psi_{max}}{\Psi_{max}|_{k\sigma=0}} \right| \approx 1 - 2[k\sigma \cos(\theta_i)]^2 \quad (1.30)$$

in the limit $K_0 L \gg 1$ and for $k\sigma < 1$ [50]. This result is consistent with physical intuition and with an analogous result derived for the average scattering coefficient of random surfaces. It also demonstrates that under appropriate approximations the relative *rms* height of the surface determines the scattering intensity in the specular direction for both fractal and random surfaces.

1.3.2.2 Scattering Cross Sections for the Approximate Case

The next three figures display the scattering cross-section results from the Kirchhoff scattering approximation for fractally rough surfaces. In each case the scattering cross section (1.29) is plotted on a logarithmic scale as a function of scattering angle θ_s in the scattering plane formed by \mathbf{k}_i and \mathbf{k}_s . Figure 1.12 displays the fundamental result of this section. Here the angular scattering is shown for the roughness fractal dimension $D_r = 1.05, 1.30, 1.50, 1.70$, respectively, from left to right and top to bottom. The frequency scaling parameter is $b = 2e/3 \approx 1.81$ and the number of tones is $N = 6$. The illuminating plane wave is incident at an angle $\theta_i = 30^\circ$ with respect to the reference plane as indicated by the arrow on the left. The *rms* height of the surface is $\sigma = 0.05\lambda$ and the patch size is $2L = 40\lambda$. Each plot is the average result of ten members of the ensemble, each with a different set of randomly chosen phases ϕ_n in (1.24) and (1.29).

As expected, the scattered energy is increasingly dispersed in angle as the roughness or fractal dimension increases. Therefore, we anticipate that this dispersion will provide a method to distinguish and classify such surfaces.

The physical basis for the spreading of scattered energy away from the specular

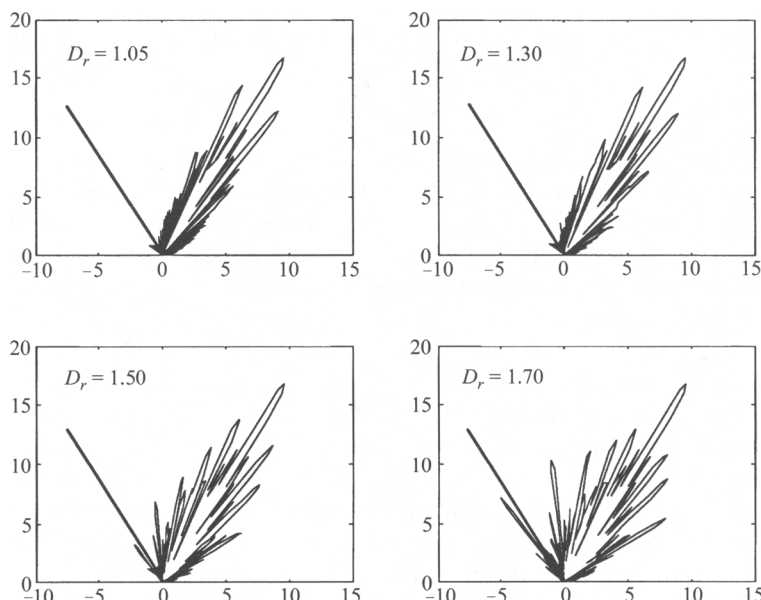


Figure 1.12 The angular variation of the scattering cross-section $d\sigma(\theta_i, \theta_s)/d\theta_s$ as a function of scattering angle θ_s for fractally corrugated surfaces with roughness fractal dimension $D_r = 1.05, 1.30, 1.50$, and 1.70 , respectively, left to right, top to bottom. The incident wave is at $\theta_i = 30^\circ$ (indicated by arrow) to the reference plane normal, and the patch size is $2L = 40\lambda$. These are polar plots with a dB scale shown for reference. [Figure adapted from “Scattering from Fractally Corrugated Surfaces,” D. L. Jaggard and X. Sun, J. Opt. Soc. Am. A, 7, 1131–1139 (1990). © 1990 Optical Society of America.]

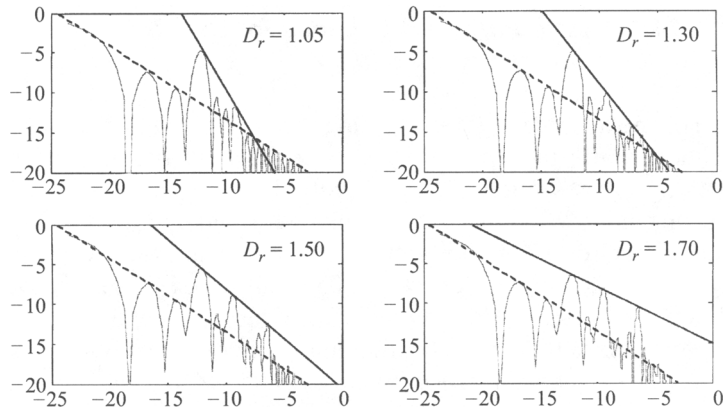


Figure 1.13 The scattering cross section $d\sigma(\theta_i, \theta_s)/d\theta_s$ as a function of $\sin[(\theta_s - 30^\circ)/2]$, both in dB scales, for roughness fractal dimension $D_r = 1.05, 1.30, 1.50$, and 1.70 , respectively, left to right, top to bottom. The incident wave is at $\theta_i = 30^\circ$ to the reference plane normal, and the patch size is $2L = 40\lambda$. These are polar plots with a dB scale shown for reference. The envelope slopes of coupling sidelobes (solid lines) vary monotonically with the fractal dimension while the background slope (dashed lines) is constant for varying D_r . [Figure adapted from “Scattering from Fractally Corrugated Surfaces,” D. L. Jaggard and X. Sun, J. Opt. Soc. Am. A, 7, 1131–1139 (1990). © 1990 Optical Society of America.]

direction with increasing fractal dimension can also be understood from conservation of momentum. From (1.24) we see that as D_r increases the surface will add larger amounts of momentum ($\sim K_0 b''$) to the momentum of the incident wave ($\sim k$), in a direction parallel to the reference plane. Therefore, to conserve momentum, the scattered wave contains power that is redirected away from the specular direction. This phenomenon is often termed *Bragg coupling*.

The angular scattering cross section for $D_r = 1.05$ in Fig. 1.12, where the roughness is minimal and the surface is near sinusoidal, shows a main beam in the specular scattering direction. The two large sidelobes, one on each side of the specular scattering lobe, are due to Bragg coupling by the dominant ($n = 0$) sinusoid in (1.24). These *coupling lobes* are characteristic of any diffraction grating. With increasing roughness, for $D_r = 1.30$ and 1.50 , additional coupling lobes emerge and their intensities grow due to the additional coupling by each significant sinusoid in the fractal function that defines the surface. The intensity of each coupling lobe approaches the same value as $D_r \rightarrow 2$. This effect can be partially observed in the plot for $D_r = 1.70$. Nulls in these plots are evident in the ensemble average and so must be due to the zeros of the sinc functions of (1.29).

In Fig. 1.13 we replot the scattering cross-section data of Fig. 1.12 for the region $30^\circ < \theta_s < 90^\circ$ as a function of $\sin[(\theta_s - 30^\circ)/2]$, both quantities shown on logarithmic scales. Two envelopes are evident in these plots. The background envelope (dashed line with slope ≈ -1) is due to the finite patch size and consists of the specularly reflected main beam and its sidelobes. The coupling lobe envelope (solid line with variable slope) is due to surface coupling and consists of the first-order coupling of the

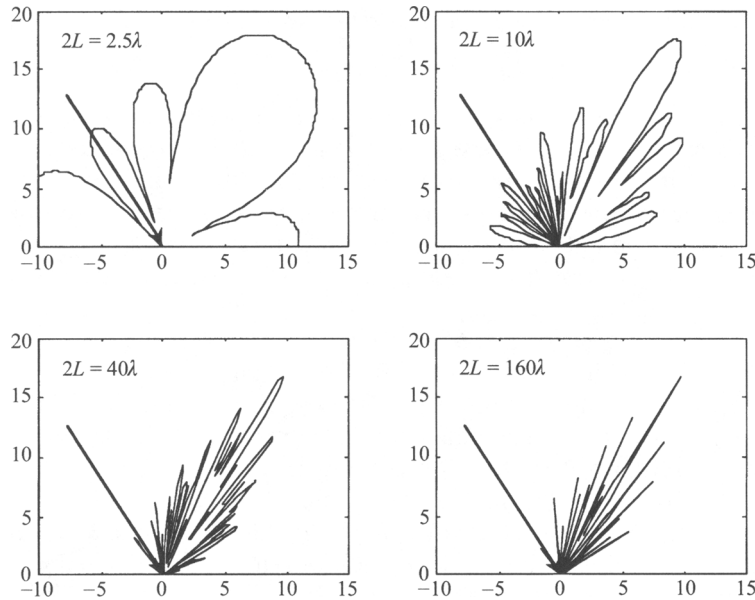


Figure 1.14 Polar plot of the angular variation of the scattering cross section $d\sigma(\theta_i, \theta_s)/d\theta_s$ as a function of scattering angle θ_s for fractally corrugated surfaces with dimension $D_r = 1.5$ and patch sizes $2L = 2.5\lambda, 10\lambda, 40\lambda$, and 160λ , from left to right, top to bottom. Here $\lambda/\Lambda_0 = 0.1$ and $\theta_i = 30^\circ$. [Figure adapted from “Scattering from Fractally Corrugated Surfaces,” D. L. Jaggard and X. Sun, J. Opt. Soc. Am. A, **7**, 1131–1139 (1990). © 1990 Optical Society of America.]

surface harmonics. This latter slope is indicative of surface roughness and is given approximately as $-[2.7(2 - D_r)]$ for the cases examined here. This result is not dissimilar to that of scattering from fractal aggregates and porous material and suggests that this slope provides a means for quantifying fractal dimension and surface roughness. An alternative measure of fractal dimension may be obtained through the integration of the scattered power in successive bands of sidelobes. Examples of this for other diffraction problems are given elsewhere [12], [15], [82–86].

The variation of scattering cross section with patch size is of interest in remote sensing and surface characterization. This information is displayed in Fig. 1.14 where polar plots of the scattering cross section are given for $D_r = 1.50$ and $2L = 2.5\lambda, 10\lambda, 40\lambda$, and 160λ . The specular scattering mainbeam width is inversely proportional to the normalized patch size. As expected, the angular scattering cross section provides less information about surface roughness as the patch size $2L$ decreases below the critical value Λ_0 since there is not enough of the fractal surface to accurately imprint its fractal signature on the illuminating wave. Likewise, as seen from Fig. 1.14 the patch must contain at least 5 to 10 wavelengths of the incident wave to accurately provide information regarding its multiscale nature. Therefore, we suggest that the relation $2L > \Lambda_0 \geq 5\lambda$ should hold to extract fractal information from multiscale surfaces.

1.3.2.3 Observations on the Approximate Case

Several observations on fractal surface scattering can be noted from the approximate results. First, the scattering intensity in the specular direction is a strong function of the *rms* height of the rough surface and has a similar functional dependence as one would expect for random surface models. Second, the roughness fractal dimension D , controls the distribution of energy among scattering lobes. This result is typical of many wave interactions with fractal structures. As the dimension increases there are more opportunities for significant Bragg coupling. Third, the spatial frequency parameter b , which determines the spacing of the surface harmonics, controls the angular separation of the coupling beams in accordance with the conservation of momentum (Bragg's law). Fourth, the slope of the coupling lobe envelope provides both a qualitative and a quantitative measure of surface roughness as expressed by D . Fifth, for accurate remote probing of fractal surfaces, the scattering patch size should be larger than the fundamental period of the fractal surface and larger than five wavelengths for significant fractal information contained in the surface to be embedded in the scattered wave. Finally, we note that the formulation for this problem is almost identical to that for diffraction by a single fractal phase screen [80]. In each case, an incident field has impressed on its phase front information about a fractal object. The wave then propagates in accordance with diffraction theory but contains encoded fractal information which can be extracted from the scattered data. Alternative viewpoints of approximate scattering using the Rayleigh approximation [51], [52] and using a perturbational approach [54] can be found elsewhere. Applications to sea and related surface scattering are also available [56], [57], [63–67], [87–96].

We turn now to an exact method that yields quantitatively similar results but can be applied to surfaces which violate some of the restrictions (e.g., moderate or large radii of curvature, relatively small surface slopes, and relatively small heights of roughness) inherent in most approximate methods including the one used here. The exact method also takes into account electromagnetic wave polarization which was neglected in the scalar Kirchhoff approximation.

1.3.3 Exact Scattering Solution

We apply the T-matrix approach or EBCM of Waterman [97–99] to the problem of the previous section—scattering of electromagnetic waves from perfectly conducting fractal surfaces. The method formulation is exact, at least in principle, when applied to periodic surfaces and has been previously applied to the case of sinusoidal surfaces [100] and random rough surfaces [101].

The T-matrix approach involves the extinction theorem in which the surface field produces a contribution inside the object that exactly cancels the incident field throughout the interior of the object. The resulting transition-matrix or T-matrix [T] relates incident and scattered fields. Details of the original method are readily available in several texts [102], [103].

Here we follow our prior work [55], [60] and expand the T-matrix method to a class of fractal surfaces characterized by the fractal function (1.24) which is subset of

the class of almost-periodic functions. Using concepts developed for waves in almost-periodic media [104], we expand the surface fields in terms of generalized Floquet modes. This allows us to find closed-form expressions for the scattering amplitudes in the TE and TM cases. Results for the angular scattering cross section are found numerically using infinite matrices truncated to the n^{th} order.

1.3.3.1 Formulation of Exact Surface Scattering Solution

The T-matrix approach starts with Green's theorem below, assuming $e^{-i\omega t}$ time-harmonic variation,

$$\begin{aligned} \psi_i(\mathbf{x}) + \iint_{S_{\text{fractal}}} [\psi(\mathbf{x}') \hat{\mathbf{n}} \cdot \nabla'_S G(\mathbf{x}, \mathbf{x}') - G(\mathbf{x}, \mathbf{x}') \hat{\mathbf{n}} \cdot \nabla'_S \psi(\mathbf{x}')] dS' \\ = \begin{cases} \psi(\mathbf{x}), & z > f_r(x) \\ 0, & z < f_r(x) \end{cases} \quad (1.31) \end{aligned}$$

where $\psi(\mathbf{x}')$ is the electric (TE or perpendicular polarization) or magnetic (TM or parallel polarization) surface field transverse to the scattering plane formed by \mathbf{k}_i and \mathbf{k}_s . Here $\psi(\mathbf{x})$ and $\psi_i(\mathbf{x})$ are the total and incident transverse fields, respectively. As before, $f_r(x)$ is the fractal function defined in (1.24). The upper inequality in (1.31) provides the total field at an arbitrary point \mathbf{x} above the conducting surface as the sum of incident and scattered fields, with the scattered fields represented by the surface integral which extends over the fractal surface S_{fractal} . The lower inequality corresponds to the extended boundary condition in which the surface field and its normal derivative give rise to a wave which cancels the incident field in the region below the surface.

The Green's function in (1.31) is the two-dimensional free-space form given by

$$\begin{aligned} G(\mathbf{x}, \mathbf{x}') &= \frac{i}{4} H_0^{(1)}(k|\mathbf{x} - \mathbf{x}'|) \\ &= \frac{i}{4\pi} \int_{-\infty}^{\infty} \frac{1}{k_z} e^{[ik_x(x-x')+ik_z|z-z'|]} dk_x \quad (1.32) \end{aligned}$$

where $H_0^{(1)}$ is the Hankel function of the first kind and zeroth order and represents an outwardly propagating cylindrical wave.

Next the surface field and the field above the surface are both expanded into generalized Floquet series. This allows the surface field coefficients in the column vector $[\alpha]$ to be written in terms of the incident field coefficients of the column vector $[a]$. The relation is

$$[a] = [Q^-][\alpha] \quad (1.33)$$

where the square matrix $[Q^-]$ has elements containing exponentials and Bessel functions related to the surface geometry. Likewise it can be shown that the scattered field coefficients in the column vector $[b]$ can also be written in terms of the column vector $[\alpha]$ as

$$[b] = [Q^+][\alpha] \quad (1.34)$$

where $[Q^+]$ is a second square matrix containing information regarding surface geometry. The formulations are slightly different for the TE and TM polarizations and are carried out explicitly elsewhere [55], [60] for the quantities $[\alpha]$, $[a]$, $[b]$, $[Q^-]$ and $[Q^+]$. The result in both cases is a T-matrix $[T]$ of the form

$$[T] = [Q^+] [Q^-]^{-1} \quad (1.35)$$

Using (1.33)–(1.35) we find

$$[b] = [T][a] \quad (1.36)$$

which relates incident and scattered field coefficients. The column vector $[b]$ contains the information from which the scattering cross sections $d\sigma(\theta_i, \theta_s)/d\theta_s$ can be calculated.

One of the major contributions of this work is the extension of the T-matrix approach from periodic surface scattering to multiscale, almost-periodic surface scattering. We turn now to these results.

1.3.3.2 Scattering Cross Sections for the Exact Case

The T-matrix numerical results of the next four figures show the scattering cross section $d\sigma(\theta_i, \theta_s)/d\theta_s$ as a function of scattering angle θ_s for a specified incident angle θ_i . These results appear to be numerically accurate in that they are self-consistent with respect to the energy balance between incident and scattered wave quantities and take into account interactions through the fifth order with little variation in the scattering results with respect to change in order. Typically we find the energy balance parameter to differ from unity by less than 0.1. Finally, in the appropriate limit, the T-matrix results approach results from both the Kirchhoff and Rayleigh approximations which provides additional validation of these results.

We first examine the comparison between the T-matrix results and those of the Kirchhoff approximation. This is followed by an examination of T-matrix results for the case where the surface profiles no longer satisfy the Kirchhoff assumptions because of increasing surface height or increasing illumination frequency. For these latter cases in which an exact formulation is needed, we also examine the effect of polarization.

The angular scattering cross sections for TE polarization shown in Fig. 1.15 demonstrate rather good agreement between the T-matrix method (solid line) and the Kirchhoff method (solid line with boxes) for the case of relatively small wavelength and *rms* surface height variations ($\lambda/\Lambda_0 = 0.2$ and $k\sigma = 0.5$). The results show that for modest fractal dimension the scattered field displays the specular peak and two large peaks due to the dominant sinusoid of the surface. The specular peaks predicted by the T-matrix and Kirchhoff methods are graphically indistinguishable. Higher spatial frequency sinusoids of the surface and the finite patch size contribute auxiliary sidelobes which appear on either side of the specular mainlobe. The Kirchhoff approximation accurately mimics the three major scattering lobes (mainlobe and two major sidelobes) and most of the smaller sidelobes found in the T-matrix calculation.

As the surface roughness and wavelength increases, the Kirchhoff assumptions are violated and this approximation technique gracefully degrades until it provides neither

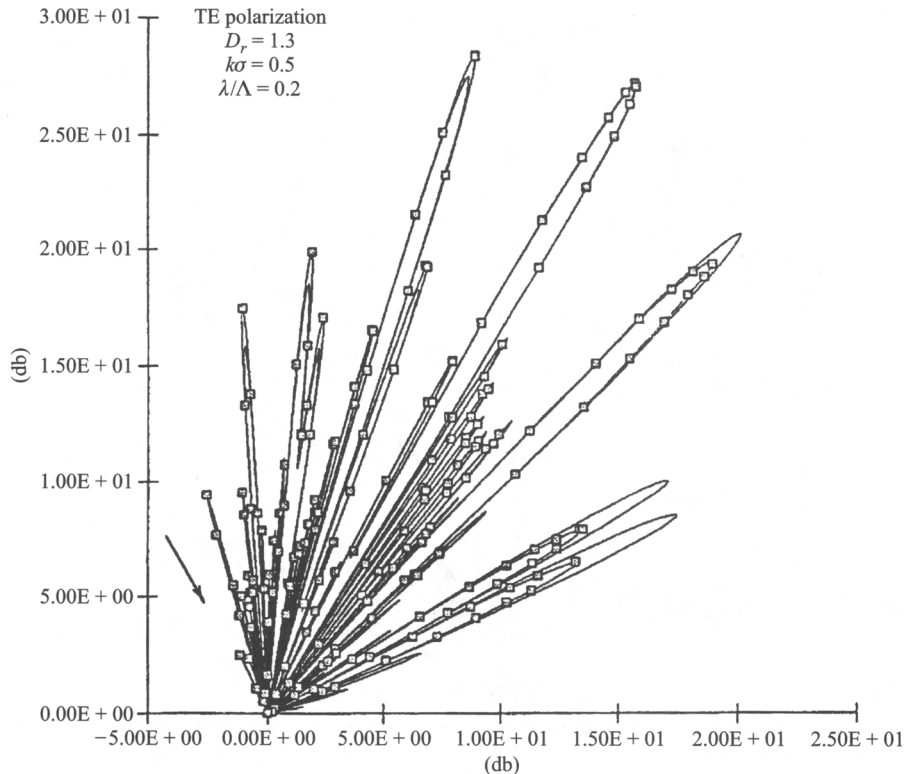


Figure 1.15 Polar plot of the angular variation of the scattering cross section $d\sigma(\theta_i, \theta_s)/d\theta_s$ as a function of scattering angle θ_s for fractally corrugated surfaces with dimension $D_r = 1.3$, spatial frequency scaling $b = 2e/3$, patch size $2L = 40\lambda$, rms height $k\sigma = 0.5$ and normalized incident wavelength $\lambda/\Lambda = \lambda/\Lambda_0 = 0.2$ for TE polarization. The incident angle $\theta_i = 30^\circ$ is indicated by the arrow at left. Kirchhoff results (solid lines with boxes) and T-matrix results (solid lines) differ by only small amounts since the Kirchhoff approximations are valid. [Figure adapted from “Scattering from Fractally Corrugated Surfaces: An Exact Approach,” S. Savaidis, P. Frangos, D. L. Jaggard and K. Hizanidis, Opt. Lett., **20**, 2357–2359 (1995). © 1995 Optical Society of America.]

a quantitatively accurate nor a qualitatively accurate picture of the TE scattering as demonstrated in Fig. 1.16. Here the Kirchhoff results (solid line with boxes) differ greatly from the exact T-matrix results (solid line) and offer no reasonable approximation either in the mainlobe region or in the far sidelobe region. In particular the Kirchhoff results do not correctly identify the mainlobe in the specular direction and place large sidelobes where none exists. This is an example of the eventual failure of an approximation method for rough surface scattering.

The next figure displays results for rms surface height and illuminating wave frequency that again significantly violate the Kirchhoff approximation. The angular

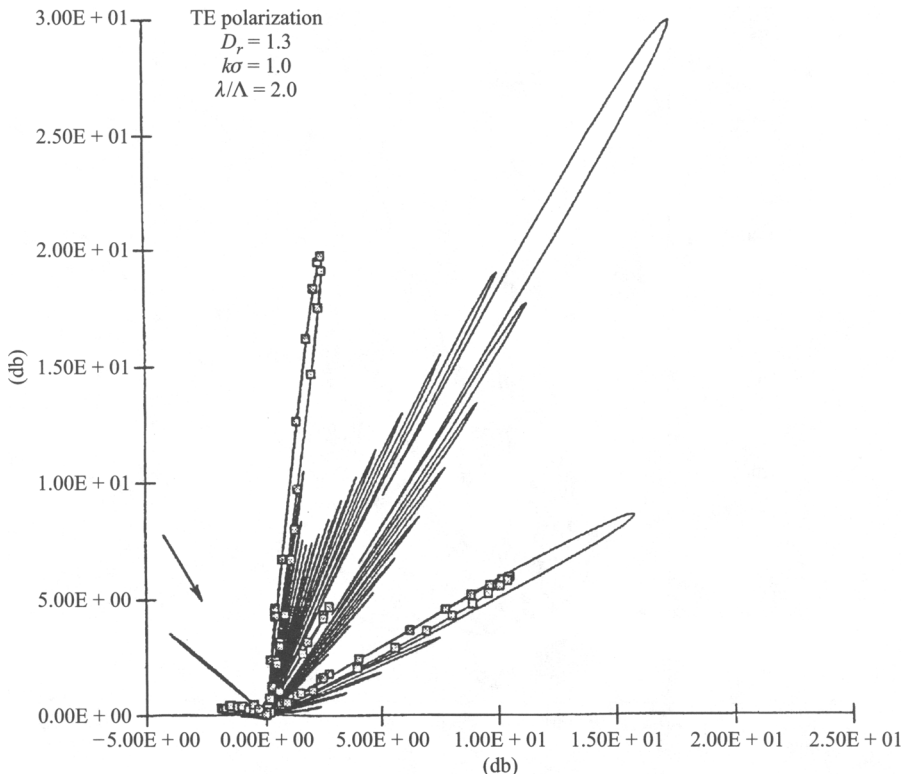


Figure 1.16 Polar plot of the angular variation of the scattering cross section $d\sigma(\theta_i, \theta_s)/d\theta_s$ as a function of scattering angle θ_s for fractally corrugated surfaces with dimension $D_r = 1.3$, spatial frequency scaling $b = 2e/3$, patch size $2L = 40\lambda$, rms height $k\sigma = 1.0$, and normalized incident wavelength $\lambda/\Lambda = \lambda/\Lambda_0 = 2.0$ for TE polarization. The incident angle $\theta_i = 30^\circ$ is indicated by the arrow at left. Kirchhoff results (solid lines with boxes) and T-matrix results (solid lines) differ significantly since the Kirchhoff approximations are violated. Note that the Kirchhoff results do not provide even a qualitative picture of the T-matrix results. [Figure adapted from “Scattering from Fractally Corrugated Surfaces: An Exact Approach,” S. Savaidis, P. Frangos, D. L. Jaggard and K. Hizanidis, Opt. Lett., **20**, 2357–2359 (1995). © 1995 Optical Society of America.]

scattering cross-section for variations in normalized rms surface height $k\sigma$ is shown in Fig. 1.17 for both TE (left side) and TM (right side) polarizations as a function of rms surface height $k\sigma$ with constant roughness fractal dimension $D_r = 1.5$. It is clear that as the rms surface height increases (bottom of figure), the role of polarization becomes more important while for small surface variations (top of figure) polarization is less important. However, the effect of polarization is subtle for all examples in this figure.

Similar results appear in Fig. 1.18 for plots of angular scattering cross-section with increasing roughness as indicated by the fractal dimension D_r , and constant rms surface height $k\sigma = 1.0$. In most cases the role of polarization is modest but greater than that displayed in the previous figure. As might be anticipated from the Kirchhoff results, the

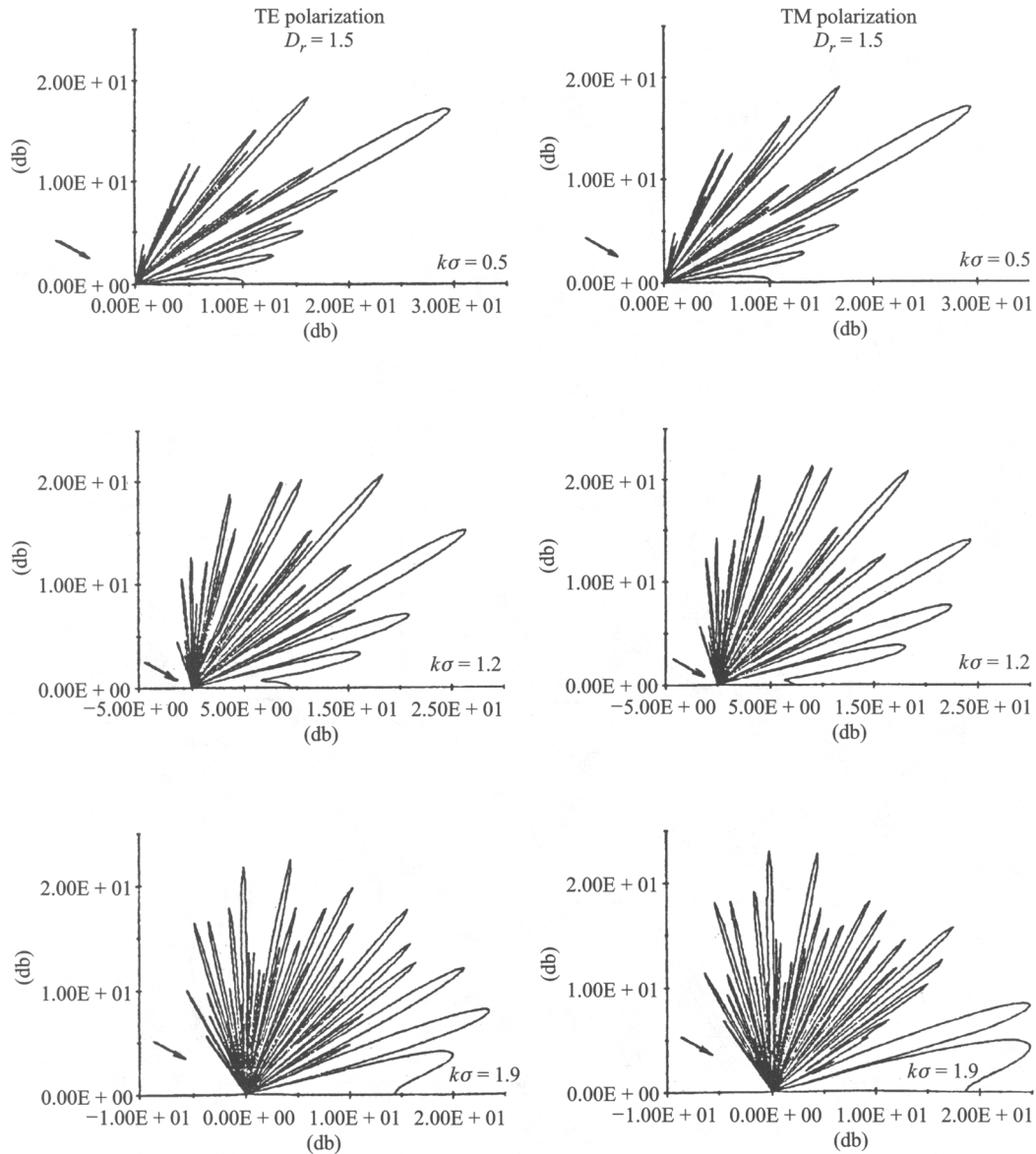


Figure 1.17 Polar plots of the angular variation of the scattering cross section $d\sigma(\theta_i, \theta_s)/d\theta_s$ as a function of scattering angle θ_s for TE (left) and TM (right) polarizations and rms surface height $k\sigma = 0.5, 1.2, 1.9$ (top to bottom) using the T-matrix approach. The fractally corrugated surfaces are characterized by dimension $D_r = 1.5$, spatial frequency scaling $b = 2e/3$, patch size $2L = 40\lambda$, normalized incident wavelength $\lambda/\Lambda_0 = 0.2$ with $N = 2$. The incident angle $\theta_i = 60^\circ$ is indicated by the arrow at left. [Figure adapted from “Scattering from Fractally Corrugated Surfaces with Use of the Extended Boundary Condition Method,” S. Savaidis, P. Frangos, D. L. Jaggard and K. Hizanidis, J. Opt. Soc. Am. A, **14**, 475–485 (1997). © 1997 Optical Society of America.]

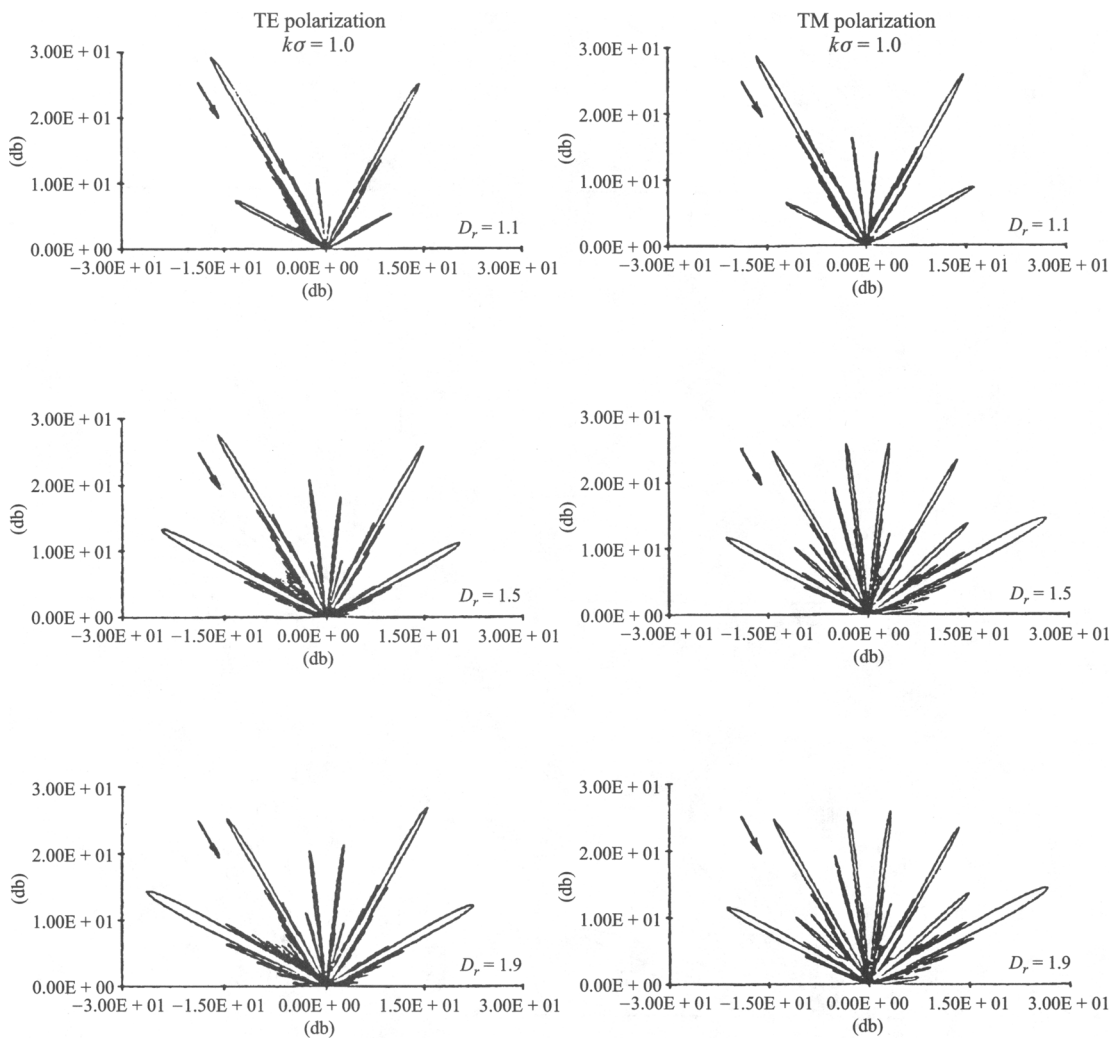


Figure 1.18 Polar plots of the angular variation of the scattering cross section $d\sigma(\theta_i, \theta_s)/d\theta_s$ as a function of scattering angle θ_s for TE (left) and TM (right) polarizations and dimension $D_r = 1.1, 1.5, 1.9$ (top to bottom) using the T-matrix approach. The fractally corrugated surfaces are characterized by rms surface height $k\sigma = 1.0$, spatial frequency scaling $b = 2e/3$, patch size $2L = 40\lambda$, normalized incident wavelength $\lambda/\Lambda_0 = 1.0$ with $N = 2$. The incident angle $\theta_i = 30^\circ$ is indicated by the arrow at left. [Figure adapted from “Scattering from Fractally Corrugated Surfaces with Use of the Extended Boundary Condition Method,” S. Savaidis, P. Frangos, D. L. Jaggard and K. Hizanidis, J. Opt. Soc. Am. A, **14**, 475–485 (1997). © 1997 Optical Society of America.]

redistribution of energy away from the specular direction also increases with dimension for these T-matrix results.

1.3.3.3 Observations on the Exact Case

The T-matrix results summarized in this chapter have extended prior results for sinusoidal and other periodic surfaces to the case of almost-periodic and fractal surfaces. This analytic extension of previous results is significant since it enlarges the family of surfaces that can be considered using T-matrix techniques. The T-matrix numerical results have been validated by comparing them to the solution for a sinusoidal surface, by comparing them to both Kirchhoff and Rayleigh results in the appropriate limit, by confirming that energy is conserved, and by examining the stability of these results with respect to variations in the number of interactions that are included in the calculation. From all of these considerations it appears the T-matrix cross sections for the surfaces examined here are accurate and consistent with known results.

These considerations suggest that for sufficiently large surface variations or sufficiently large fractal dimension the polarization of the illuminating wave may play an important role. In particular there are more rapid variations in the scattering cross section for the TM case when compared to the TE case. This is consistent with the polarization effects for scattering from a variety of non-fractal objects. However, for none of the examples considered here are the scattering cross sections radically different for TE and TM polarizations. Instead the effects tend to be modest and in some cases rather subtle. Larger effects will occur as the roughness, number of tones in the surface function, frequency of illumination, and *rms* surface height increase. One of the research problems that remains to be solved is to find the general relation between the dispersion of power away from the specular direction and the fractal dimension D_r for arbitrary values of corrugation depth, surface slope, and frequency.

1.4 REFLECTION FROM CANTOR SUPERLATTICES

We now consider the reflection and transmission properties of fractal superlattices (multilayers) characterized by generalized Cantor bars. As in wave interactions with fractally rough surfaces and other structures based on fractal geometry, we see that an electromagnetic wave reflected from one of these superlattices is distinctively imprinted with the fractal characteristics of the superlattice. Our interest is in how this occurs and what information about the superlattice can be retrieved from the reflected wave.

We are able to exploit the fractal nature of these superlattices so that the structure of the solution parallels that of the fractal. Additionally, we can explain the main features of frequency-domain reflection data using physically motivated first-order arguments. This aids us in extracting from the reflection data information about the stage of growth S , number of gaps n_{gaps} , and fractal dimension D_s describing the superlattice. We also briefly discuss time-scale methods that use wavelets to extract fractal descriptors from time-domain reflection data.

1.4.1 Problem Geometry

We consider an electromagnetic wave incident upon a superlattice derived from a polyadic (multigap) Cantor bar C constructed as described in Section 1.2.4.2. A superlattice infinite in y and z may be constructed from C by defining the refractive index

$$n(x) = \begin{cases} n_1, & x \in C \\ n_0, & x \notin C \end{cases} \quad (1.37)$$

We take C to be a finite stage of growth Cantor bar, since as S increases the number of interfaces becomes large and the reflection coefficient approaches unity. As above, we will still refer to the “fractal dimension” of these prefractals and use the similarity dimension D_s of the limiting set to quantify this descriptor.

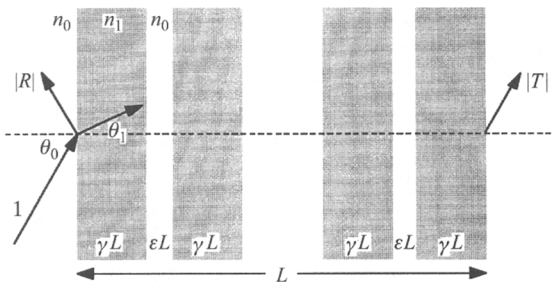


Figure 1.19 Electromagnetic wave obliquely incident from the left on a three-gap Cantor superlattice of length L at the first stage of growth. The angle of incidence and propagation in regions of refractive index (white) is θ_0 , while the angle of propagation through layers of index n_1 (shaded) is θ_1 given by Snell’s law. The individual refractive layers are of length γL and the outer gaps are of length εL . [Figure after [77].]

The problem geometry is shown in Fig. 1.19. An electromagnetic wave is incident from the left on the superlattice at an angle θ_0 from normal. The angle θ_1 from normal of propagation within the regions of index n_1 is given by Snell’s law. We derive expressions for the magnitudes $|R|$ and $|T|$ of the reflected and transmitted fields using a recursive method that incorporates the symmetry of the superlattice structure.

1.4.2 Doubly Recursive Solution

The reflection and transmission coefficients of general superlattices may be computed using the chain-matrix method. However, for the family of superlattices defined above, we look for more efficient methods which might exploit the symmetry of these structures. We have developed a doubly recursive method of solution in which both recursions make use of the fractal structure to decrease the computational burden of calculating reflection and transmission coefficients [75], [77].

The first recursion is used to obtain the form for the coefficients of a collection of N identical objects arranged as the scaled copies of C are arranged within $[0, L]$. Following Knittl [105], we temporarily replace each of the N sub-multilayers with a single interface whose reflection and transmission coefficients x and y represent those of the entire sub-multilayer. We then separate the front interface from the back $N - 1$ interfaces and express the coefficients of the N interfaces in terms of the coefficients of the 1st interface and the group of $N - 1$ interfaces. The second step in the recursion gives the coefficients of the back $N - 1$ interfaces in terms of the second interface and the remaining $N - 2$ interfaces. This is repeated until only a single interface, with coefficients x and y , remains.

Formally, the reflection and transmission coefficients of $N = n_{\text{gaps}} + 1$ interfaces are of the forms

$$\text{gen}_r(n_{\text{gaps}}) = \frac{x + (y^2 - x^2)\text{gen}_r(n_{\text{gaps}} - 1)\exp(2in_0 k \alpha_i L \cos \theta_0)}{1 - x\text{gen}_r(n_{\text{gaps}} - 1)\exp(2in_0 k \alpha_i L \cos \theta_0)} \quad (1.38)$$

$$\text{gen}_t(n_{\text{gaps}}) = \frac{y\text{gen}_t(n_{\text{gaps}} - 1)\exp(in_0 k \alpha_i L \cos \theta_0)}{1 - x\text{gen}_r(n_{\text{gaps}} - 1)\exp(2in_0 k \alpha_i L \cos \theta_0)} \quad (1.39)$$

respectively, for $n_{\text{gaps}} \geq 1$ and k the free space wavenumber of the illuminating wave. Here the α_i ($i = 1, 2, \dots, n_{\text{gaps}}$) denote the gap sizes normalized to the total length L and θ_0 is the angle of propagation with respect to the interface normal in the gaps. Relations (1.38–1.39) are subject to the initial conditions

$$\text{gen}_r(0) = x \quad (1.40)$$

and

$$\text{gen}_t(0) = y \quad (1.41)$$

corresponding to a single sub-multilayer.

Equations (1.38–1.41) are used in the first recursion to generate the reflection and transmission functions

$$g_r[x, y, L] = \text{gen}_r(n_{\text{gaps}}) \quad (1.42)$$

and

$$g_t[x, y, L] = \text{gen}_t(n_{\text{gaps}}) \quad (1.43)$$

for an n_{gaps} -gap Ca7ntor superlattice whose sub-multilayers have reflection and transmission coefficients x and y .

The dummy coefficients x and y in Eqs. (1.42–1.43) must now be replaced by the actual reflection and transmission coefficients of the sub-multilayers. We do this in the second recursion, with the fractal structure of the superlattice allowing us to write x and y as the coefficients of the superlattice at the previous stage of growth and of thickness γL . We thus have the reflection coefficient of the superlattice of thickness L generated by the stage S Cantor bar given by

$$R(S, L) = g_r[R(S - 1, \gamma L), T(S - 1, \gamma L), L] \quad (1.44)$$

with the corresponding transmission coefficient given by

$$T(S, L) = g_t[R(S - 1, \gamma L), T(S - 1, \gamma L), L] \quad (1.45)$$

When $S = 1$, the coefficients of the sub-multilayers no longer have the same form as that of the whole multilayer; they are instead simply the coefficients of a single dielectric slab of index n_1 embedded in media of index n_0 . This leads to the initial conditions

$$R(0, d) = \frac{r_{01} + (t_{01} t_{10} - r_{01} r_{10})r_{10} \exp(2in_1 kd \cos \theta_1)}{[1 - r_{10} r_{10} \exp(2in_1 kd \cos \theta_1)]} \quad (1.46)$$

and

$$T(0, d) = \frac{t_{01} t_{10} \exp(in_1 kd \cos \theta_1)}{1 - r_{10} r_{10} \exp(2in_1 kd \cos \theta_1)} \quad (1.47)$$

where

$$r_{ij} = -\frac{\hat{n}_i - \hat{n}_j}{\hat{n}_i + \hat{n}_j} \quad (1.48)$$

and

$$t_{ij} = \frac{2\hat{n}_i}{\hat{n}_i + \hat{n}_j} \Theta_{ij} \quad (1.49)$$

are the Fresnel reflection and transmission coefficients, respectively, for an interface between media of refractive indices n_i and n_j . Here

$$\Theta_{ij} = \begin{cases} \cos \theta_i / \cos \theta_j & \text{for } \parallel \text{ or TM polarization} \\ 1 & \text{for } \perp \text{ or TE polarization} \end{cases} \quad (1.50)$$

$$\hat{n}_i = \begin{cases} n_i / \cos \theta_i & \text{for } \parallel \text{ or TM polarization} \\ -n_i \cos \theta_i & \text{for } \perp \text{ or TE polarization} \end{cases} \quad (1.51)$$

In all of the work reported here, we take $n_0 = 1$ and $n_1 = 1.5$.

These relations (1.38–1.51) give the reflection and transmission coefficients for the superlattice generated by any Cantor bar in this family (D_s , S , n_{gaps} , and ε arbitrary), with any values for the refractive indices n_0 and n_1 , either polarization, and any angle of incidence θ_0 . For triadic, single-gap, and other three-gap Cantor bars, these relations imply previously obtained results [68], [70], [75].

1.4.3 Results

1.4.3.1 Twist Plots

Using the expressions derived above, we plot the magnitude $|R|$ of the reflection coefficient for a Cantor superlattice against the normalized frequency kL of the incident wave in the left of Fig. 1.20. The curves shown are for $D_s = 3/4$, $n_{gaps} = 3$, and $\varepsilon = 0.1, 0.06, 0.02$ (top to bottom).

The differences between the plots in the left of Fig. 1.20 indicate that changes in ε have an effect on the reflection data, but these plots do not give a physical understanding of these changes. As one of our primary interests is the effect of lacunarity on the reflection coefficient, we use the *twist plots* introduced in [75] to investigate the relationship between this fractal descriptor and the scattering properties of the structure. In these plots, we show $|R|$ as a function of both normalized frequency kL and lacunarity parameter ε , with dark values representing minimal reflection and light values large reflection. The twist plot for $D_s = 3/4$ and $n_{gaps} = 3$ and $S = 1$ is shown in the right of Fig. 1.20, with dashed lines indicating the ε values corresponding to the plots on the left. Here, as in other twist plots, the bottom edge of the twist plot is the maximum lacunarity case $\varepsilon = 0$.

One of the most prominent features of the twist plot in Fig. 1.20 and of twist plots in general is the clearly visible null structure which gives the plots their twisting appearance. These dark lines, representing vanishing reflection, may be classified in

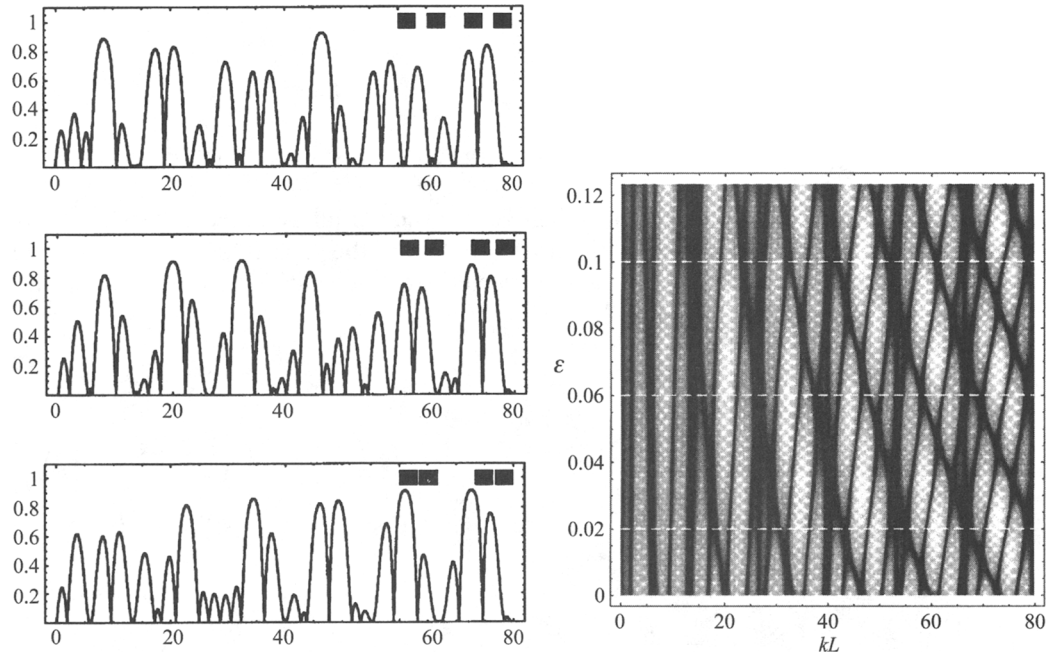


Figure 1.20 Plots of $|R|$ as a function of kL (left) with $\varepsilon = 0.1, 0.06, 0.02$ (top to bottom) for a three-gap Cantor bar with $D_s = 3/4$ and $S = 1$, and the twist plot (right) for this Cantor bar, with dashed lines indicating the values of ε for the plots at left. [Figure from “Fractal Superlattices: A Frequency Domain Approach,” A. D. Jaggard and D. L. Jaggard, presented at the PIERS (Progress in Electromagnetics Research Symposium) 1998 Meeting, Nantes, France (July 13–17, 1998). © 1998 Jaggard and Jaggard.]

three families of non-intersecting nulls. These are the *vertical nulls*, running from the top to bottom of the twist plots, the *arc nulls*, running from the upper left to lower right, and the *striation nulls*, running from the lower left to upper right. We will first explain these nulls through first-order arguments, linking them to ε , and then use them as landmarks in assessing the effects of changes in stage of growth, fractal dimension, and number of gaps.

1.4.3.2 Nulls and Their Structure

We now consider the first-order interactions which cause these three families of nulls, and derive equations predicting the nulls from these interactions. The first family of nulls is the vertical nulls, which are independent of the lacunarity parameter ε . These nulls are caused by destructive interference between the front and back faces of individual slabs of index n_1 as shown in the top of Fig. 1.21. The distance γL between these interfaces is independent of ε . The reflection from the front and back face will be out of phase (noting the sign change in the reflection off the back

interface) for values of kL given by

$$kL|_{\text{vertical nulls}} = \frac{m\pi}{\tilde{n}_1 \gamma} \quad (m = 1, 2, 3, \dots) \quad (1.52)$$

All N^S layers within the superlattice produce this null simultaneously, further reinforcing it.

The arc nulls arise from a collective destructive interference between the front faces of the individual layers within the front half of the superlattice. This occurs when the sum of the phases of the waves reflected from the sub-bar front faces is zero as shown in the middle of Fig. 1.21 or when kL satisfies

$$kL|_{\text{arc nulls}} = \frac{\left(2m + \frac{2l}{\left[\frac{N}{2}\right]}\right)}{2\tilde{n}_1 \gamma + 2\epsilon} \pi \quad \left(m = 1, 2, 3, \dots; \quad l = 1, 2, \dots, \left[\frac{N}{2}\right] - 1\right) \quad (1.53)$$

We observe that this interference occurs at the same time as the same collective

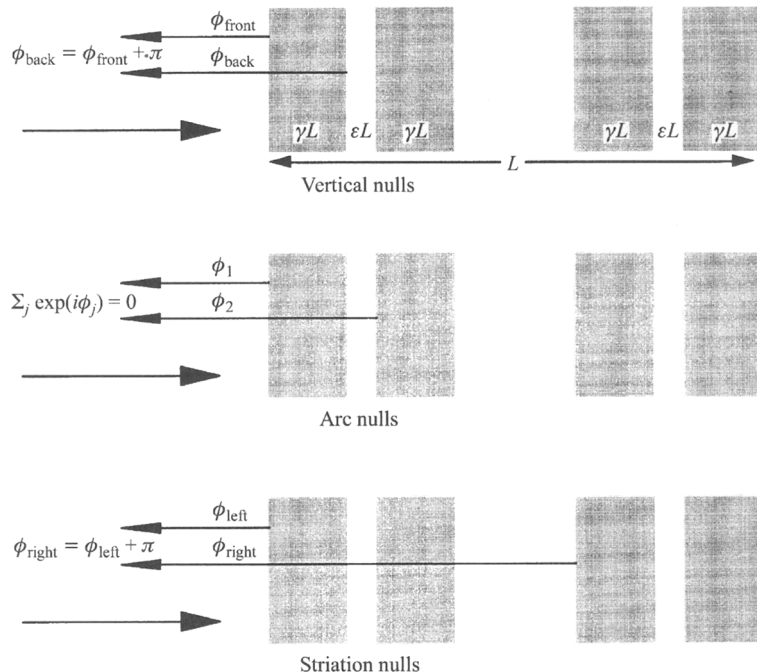


Figure 1.21 Diagram of the three first-order interferences which generate the vertical nulls, arc nulls, and striation nulls (top to bottom). Here, the ϕ 's are the phases of waves reflected from the sub-bar surfaces. The vertical nulls are caused by the destructive interference between the front and back surfaces of individual sub-bars. The arc nulls are due to the collective destructive interference from front, or back, surfaces of neighboring sub-bars. Striation nulls arise from the destructive interference from the front, or back, surface of corresponding sub-bars on either side of the Cantor bar center. [© 1999 Jaggard and Jaggard.]

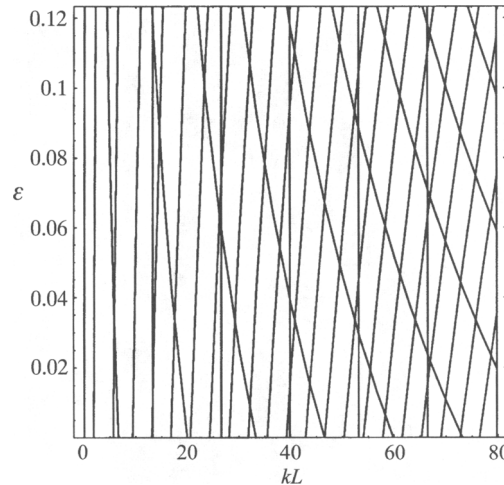


Figure 1.22 Null structure predicted by first-order analysis for the three-gap Cantor bar with $D_s = 3/4$ at the first stage of growth. Compare with the twist plot for this Cantor bar shown in Fig. 1.20. [Figure taken from “Scattering from Fractal Superlattices with Variable Lacunarity,” by A. D. Jaggard and D. L. Jaggard, J. Opt Soc. Am A, **15**, 1626–1635 (1998). © 1998 Optical Society of America.]

destructive interference within the back faces in the front half of the superlattice, the front faces in the back half, and the back faces in the back half.

The striation nulls are caused by destructive interference between the front (back) face of the i^{th} slab in the front half of the superlattice and the front (back) face of the i^{th} slab in the back half of the superlattice as pictured in the bottom of Fig. 1.21. These nulls are described by the equations

$$kL|_{\text{striation nulls}} = \frac{(2m+1)\pi}{\left(N - \left\lfloor \frac{N}{2} \right\rfloor\right)\tilde{n}_1\gamma + 1 - N\gamma - \left(\left\lfloor \frac{N}{2} \right\rfloor - 1\right)\epsilon} \quad (m = 1, 2, 3, \dots) \quad (1.54)$$

The interference occurs simultaneously for all such face pairs, reinforcing the striation nulls.

The null structure predicted by (1.52–1.54) is shown in Fig. 1.22 for a three-gap Cantor set with dimension $D_s = 3/4$ at stage of growth $S = 1$. We observe the close agreement between the nulls predicted by the first-order analysis and those shown in the corresponding twist plot in Fig. 1.20.

1.4.3.3 Polarization

Equations (1.50–1.51) allow the relations developed above for the reflection and transmission coefficients to be used for oblique angles of incidence, and we now consider the effect of polarization on the reflection data, again using twist plots to display the magnitude of the reflection coefficients.

Comparing twist plots for the parallel (TM) and perpendicular (TE) polarizations as shown in Fig. 1.23, we see that the parallel polarization reflection coefficient (left) is smaller than that for the perpendicular case (right). This is expected from the results for a half-space or a single refractive slab. As θ_0 nears the Brewster angle [= $\arctan(n_1/n_0) \approx 56^\circ$] the reflection coefficient vanishes for parallel polarization, while for grazing incidence the magnitude approaches unity.

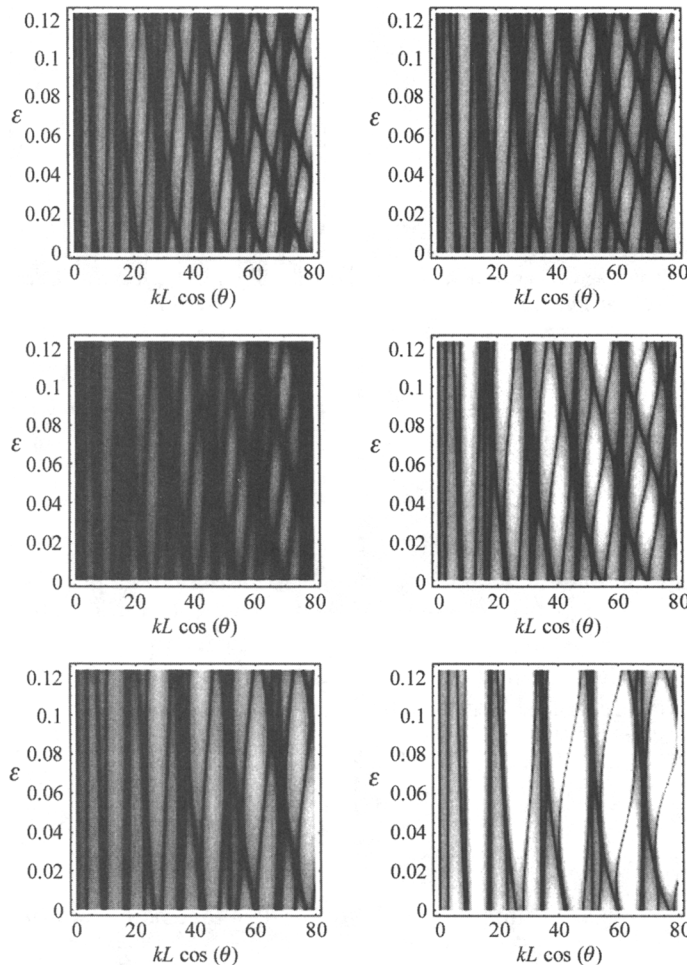


Figure 1.23 Twist plots of the absolute value of the reflection $|R|$ for the three-gap, first-stage Cantor bar with $D_s = 3/4$. These twist plots are for oblique incidence of $\theta_0 = 30^\circ, 50^\circ$, and 70° (top to bottom) for parallel (left) and perpendicular (right) polarizations. Note the decrease in reflection near the Brewster angle ($\theta_0 \approx 56^\circ$) in the middle plot in the left column. [Figure taken from “Scattering from Fractal Superlattices with Variable Lacunarity,” A. D. Jaggard and D. L. Jaggard, *J. Opt. Soc. Am. A*, **15**, 1626–1635 (1998). © 1998 Optical Society of America.]

Although the reflection coefficient may differ by large factors between the two polarizations, we observe that the null structures are essentially the same for the perpendicular and parallel cases. This suggests that the null structure is a useful tool for analyzing the reflection coefficient, regardless of polarization. The null structure does, however, change with angle of incidence, as an increase in θ_0 represents an increased path length in each layer of the superlattice, effectively stretching the null structure along the kL axis. Other examples are given in the literature [77].

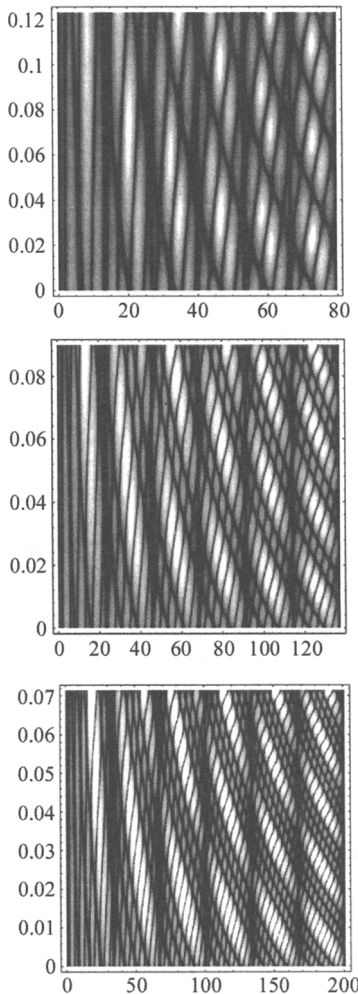


Figure 1.24 Twist plots for $n_{\text{gaps}} = 3, 5$, and 7 (top to bottom). Here $D_s = 3/4$ and $S = 1$. Note the grouping of the arc nulls as the number of gaps increases. [Figure adapted from “Scattering from Fractal Superlattices with Variable Lacunarity,” A. D. Jaggard and D. L. Jaggard, J. Opt Soc. Am A, **15**, 1626–1635 (1998). © 1998 Optical Society of America.]

1.4.4 Fractal Descriptors: Imprinting and Extraction

1.4.4.1 Frequency-Domain Approach

Number of Gaps n_{gaps} . We are able to retrieve the value of n_{gaps} through visual inspection of the twist plots. The arc nulls are grouped in sets of $\lfloor (N - 1)/2 \rfloor$, with these groups separated by regions without arc nulls. This is illustrated in Fig. 1.24 where twist plots are shown for $n_{\text{gaps}} = 3, 5$, and 7 (top to bottom); these contain arc nulls in sets of 1, 2, and 3, respectively. We may explain this grouping from first principles and (1.52–1.54) [106]. For Cantor bars with n_{gaps} even and thus a central bar instead of a central gap, we see evidence of this geometrical change in the null structure [77]. We may use this to determine the parity of n_{gaps} , and along with the grouping of the arc nulls determine the exact value of n_{gaps} .

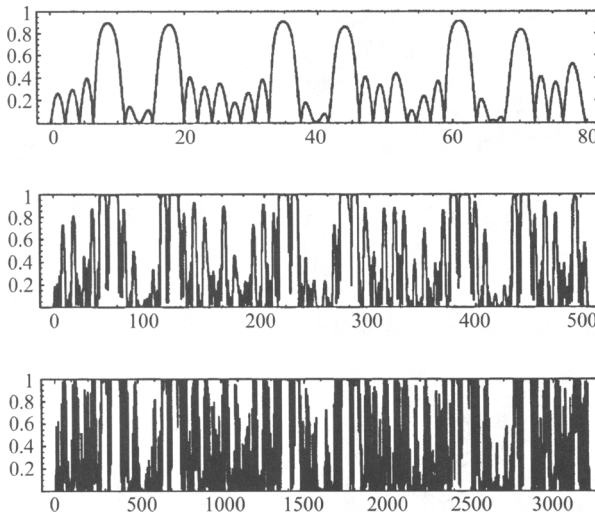


Figure 1.25 Plots of $|R|$ as a function of kL for $S = 1, 2, 3$ (top to bottom). Each stage reflection is rescaled by $1/\gamma$ in kL . Here $D_s = 3/4$, $n_{\text{gaps}} = 3$, and $\varepsilon = \varepsilon_{\max}$ for minimum lacunarity. Note the similar overall structure, overlaid with increasingly rich detail as S increases.

Stage of Growth S . At stage of growth S , the intervals in the Cantor bar are of length $\gamma^S L$. Thus with increasing stage of growth, we see increasingly fine structure in the superlattice and richer structure in the twist plots. In Fig. 1.25 we plot the reflection coefficient for superlattices with $D_s = 3/4$, $n_{\text{gaps}} = 3$ for stages of growth $S = 1, 2, 3$ (top to bottom), and with minimum lacunarity $\varepsilon = \varepsilon_{\max}$. Note that the kL axis has been rescaled by $1/\gamma$ between each stage; this corresponds to the scaling by γ of the smallest structure present in the superlattice. Here the reflection plot at stage of growth S exhibits structure similar to the (rescaled) reflection plot at stage of growth $S + 1$. Knowing the length L and n_{gaps} of the superlattice it appears the stage of growth can be extracted from the reflection data.

Fractal Dimension D_s . From (1.52–1.54), we see that the locations of all three families of nulls are functions of γ and, in the case of the arc and striation nulls, N . Since these quantities determine D_s , we expect that variations in fractal dimension would have some effect on the null structure of twist plots. As demonstrated in [77], changes in D_s are seen in the corresponding twist plots, indicating that the fractal dimension of the superlattice is imprinted on the reflected wave. This is also evident from effective medium theory, which suggests that low-frequency reflection data will contain information about the average index of the superlattice since low-frequency waves in the superlattice “see” the refractive index averaged over the entire superlattice. With knowledge of the number of gaps, stage of growth, and values of n_0 and n_1 , we may compute D_s from the average index of the superlattice.

We may consider the behavior at $kL = 0$ of the expression obtained above for the reflection coefficient to retrieve the average index of the superlattice and hence D_s [106], [107]. Preliminary results using this method are shown in Table 1.2 for a three-gap Cantor bar with $D_s = 1/2, 3/4, 9/10$ and $S = 1, 2, 3$. We are able to extract the value of D_s from the reflection data independent of the value of the lacunarity parameter ε .

TABLE 1.2 Values of Fractal Dimension Retrieved from Three-Gap Superlattices for Stages of Growth $S = 1, 2, 3$ and $D_s = 1/2, 3/4, 9/10$

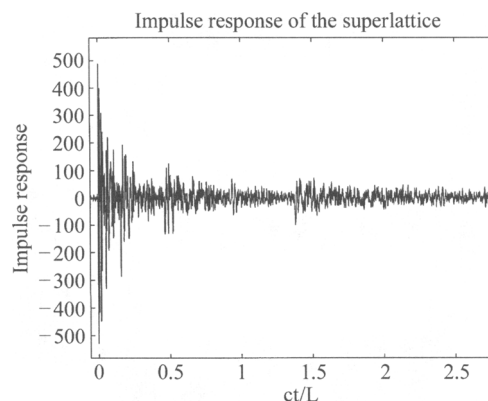
D_s	Stage 1	Stage 2	Stage 3
1/2	0.529	0.519	0.513
3/4	0.778	0.775	0.771
9/10	0.915	0.914	0.913

1.4.4.2 Time-Scale Approach

Here, we briefly consider an alternative approach to the frequency-domain discussion above by using the impulse response of a Cantor superlattice and a time-scale analysis. We expect that the finer structure present in Cantor superlattices at high stages of growth will also be seen in their time-domain response and this is indeed true for continuous Weierstrass profiles [108]. The time-scale method we consider has recently been developed using wavelet analysis to extract the stage of growth and fractal dimension from time-domain data of Cantor superlattices [109], [110], [113]. This work has made use of the natural connection between the multiple scales present in fractal structures, and thus in their electromagnetic signatures, and the multiscale analysis for which wavelets and wavelet transforms are ideally suited.

We show that when the hierarchical structure of a wavelet-transform modulus maxima is revealed in time-scale data, this structure displays the construction rule of the Cantor set that governs the geometry of the superlattices. As an example we consider the wavelet analysis of a triadic Cantor superlattice at stage of growth $S = 6$. As displayed in Fig. 1.26 its time-domain response to a narrow width Gaussian impulse consists of a series of several large peaks followed by a series of smaller peaks which eventually decay. The peaks are due to the numerous multiple reflections inherent in this superlattice. For this example we choose an interrogating impulse

Figure 1.26 Impulse response of a triadic Cantor superlattice for $S = 6$. Here $L/\tau c = 900$ where c is the vacuum speed of light and τ is the temporal standard deviation of the incident Gaussian pulse. The pulse width is chosen to be on the order of the inverse of the highest spatial frequency of the superlattice. [Figure adapted from “Fractal Superlattices and Thier Wavelet Analyses,” H. Aubert and D. L. Jaggard, Optics Comm., 149, 207–212 (1998). © 1998 Elsevier Science B.V.]



width close to the inverse of the highest spatial frequency of the superlattice. The incident wave can then access its finest structure. The continuous wavelet transform [111] of the impulse response is given in Fig. 1.27, showing both the modulus of the wavelet transform (top) and the maxima “skeleton” (bottom).

The wavelet skeleton displays the existence of a hierarchical distribution of singularities which in turn indicates both the stage of growth and fractal dimension. The stage of growth can be found from the number of hierarchical structures present in the skeleton. This skeleton “grows” from the bottom of the plot as the fractal is grown from one stage to the next and additional branching of the wavelet skeleton takes place. Thus the number of hierarchical levels in the wavelet plot reveals the stage of growth S if there is sufficient resolution in both the incident impulse and the wavelet analysis. This result appears to be valid for a variety of values of S and D_s as demonstrated in a series of examples examined recently [110] (not shown here).

Likewise, we note that a wavelet dimension D_w can be defined from the continuous wavelet transform and its associated skeleton through the scaling apparent in the hierarchical structure [109], [110], [113] (see Fig. 1.27). For refractive indices $n_0 = 1$ and $n_1 < 3.0$, the wavelet dimension is found to be almost identical to the similarity dimension D_s for a particular family of Cantor superlattices formed by

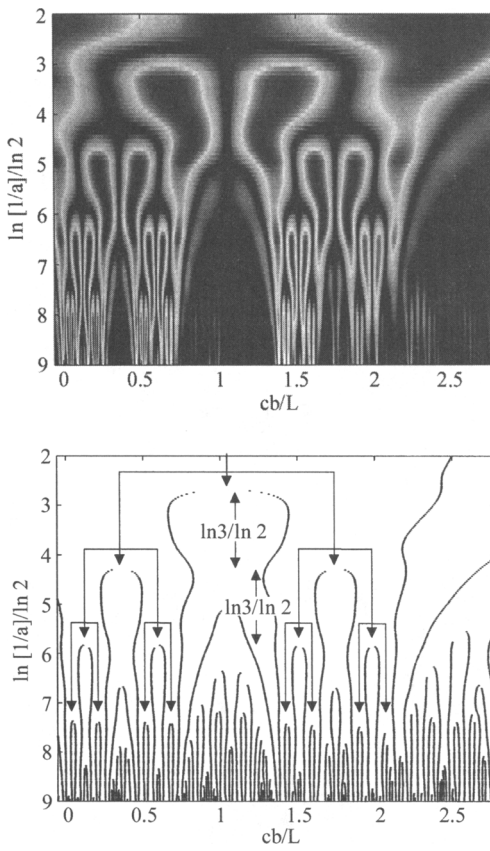


Figure 1.27 Modulus (top) of the continuous wavelet transform of the impulse response shown in Fig. 1.26 (black is zero). Here a is the scale parameter and b is the time parameter. The mother wavelet is the second derivative of the Gaussian function. Maxima (bottom) or skeleton of the wavelet transform modulus shown in the top plot. Each point indicates the location in time-scale domain of a maximum. A hierarchical structure of some wavelet maxima emerges clearly and reveals the construction rule of the associated Cantor set. The arrows indicate the branchings of such a structure (note that the scale factor between two successive branchings is constant). Here $D_s = \ln 2/\ln 3$ which is apparent from the skeleton. [Figure taken from “Fractal Superlattices and Thier Wavelet Analyses,” H. Aubert and D. L. Jaggard, Optics Comm., **149**, 207–212 (1998). © 1998 Elsevier Science B.V.]

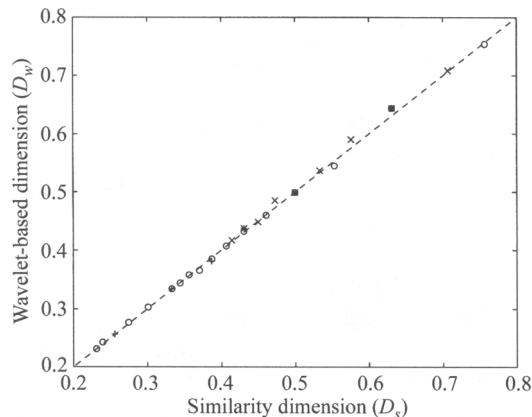


Figure 1.28 Wavelet-based dimension D_w as a function of the similarity dimension D_s for a class of Cantor superlattices: (+) $M - P = 2$, (○) $M - P = 4$ and (x) $M - P = 6$. Here each Cantor superlattice is constructed from a medium of index n_1 that is divided into M segments with the middle P segments removed and replaced with index n_0 . [Figure taken from “Fractal Superlattices and Thier Wavelet Analyses,” H. Aubert and D. L. Jaggard, Optics Comm., **149**, 207–212 (1998). © 1998 Elsevier Science B.V.]

taking a refractive bar of index n_1 , dividing it into M segments and removing the middle P segments and replacing these segments with index n_0 . A plot of the wavelet dimension D_w found from the continuous wavelet transform as a function of the similarity fractal dimension D_s used in the superlattice construction for some 25 examples of these superlattices is shown in Fig. 1.28. For these cases it appears the time-scale method is very useful for analyzing a variety of Cantor superlattices.

We see that the time-scale approach is a powerful method for examining fractal structures and appears to be inherently suited to extracting fractal descriptors from impulse response data. We also note its use in the analysis of slightly rough surfaces [112].

1.4.5 Observations on Superlattice Scattering

There are several results that should be noted. First, analytic expressions for the reflection and transmission coefficients of a family of Cantor superlattices are given as functions of fractal dimension, lacunarity, number of gaps, stage of growth, angle of incidence, and polarization. The scattering results are developed from a doubly recursive technique that efficiently yields numerical results. This method exploits the dilation symmetry of the structures so that the symmetry of the structure is mirrored in the symmetry of the calculations. Second, the concept of lacunarity is introduced to form increasingly diverse families of midpoint-symmetric polyadic Cantor sets. Lacunarity is connected to the geometric spacing of the associated Cantor set by a relation whose behavior matches our expectations for this descriptor. Third, the scattering results appear to be best summarized by a series of twist plots, particularly their null structure which is simply related to the geometry through interference arguments. Fourth, frequency-domain and time-scale approaches both appear to offer excellent ways to extract fractal descriptor information from the scattering data. For example, we find that fractal dimension, stage of growth and number of gaps can be found from reflection data using these methods. Both of these approaches are topics of continuing research.

1.5 CONCLUSION

Here we provide a brief introduction to fractal geometry, sets, and descriptors and summarize several aspects of *fractal electrodynamics*—the study of the interaction of electromagnetic waves with fractal structures. In this chapter our emphasis has been on the scattering of electromagnetic waves from fractally corrugated surfaces and fractal superlattices. In each case we have investigated methods through which fractal structures imprint their characteristic geometry on scattered waves, and techniques by which these waves can be made to yield the fractal descriptors of the scatterer.

For scattering from fractal surfaces we find that the fractal dimension is simply related to the scattering cross-section under the Kirchhoff approximation. A similar result holds under the Rayleigh approximation. The same results are evident for exact calculations of scattering cross-section in the case where the corrugation height is small or modest and the fractal dimension not too large. Likewise, similar trends appear in the exact case when approximate methods fail. However, simple connections between fractal dimension and cross section have not been found in the case of arbitrarily large corrugations or large fractal dimension, although it is quite possible they exist. An added complexity and opportunity for remote sensing is provided by the increasing role of polarization for high frequency, large dimension, or large corrugation.

For superlattices we find that many fractal descriptors are embedded in the scattering data in recognizable ways. We pay particular attention to the effect of lacunarity, “gappiness,” or texture on scattering parameters. From frequency-domain data we find methods of extracting not only the fractal dimension but also the number of gaps and stage of growth for these Cantor superlattices. In an alternative approach, we review methods by which time-scale analyses of the superlattice impulse response may also be used to investigate the properties of such multilayers. We expect the wavelet methods will be a powerful tool for fractal scattering analysis, the idea being to use multiscale analytical tools to examine multiscale structures. From our initial results the concept appears to be most promising.

Although relatively young, fractal electrodynamics has already yielded useful and intriguing results in a number of areas covering the microwave, millimeter wave and optical regimes. We anticipate additional applications to the synthesis of new devices and in reaching a deeper understanding of wave interactions with multiscale structures. The optimal use of lacunarity and perhaps other descriptors in these problems remains an open question but appears to offer a useful additional degree of freedom in the design of fractal devices. As one particularly promising case, antenna elements and arrays which follow in subsequent chapters provide several examples of applications of fractals to radiation problems. For the case of fractal arrays we again find the concept of lacunarity to be useful.

REFERENCES

- [1] D. L. Jaggard, “On Fractal Electrodynamics,” in *Recent Advances in Electromagnetic Theory*, H. N. Kritikos and D. L. Jaggard, eds., Springer-Verlag, New York, 1990, pp. 183–224.
- [2] D. L. Jaggard, “Fractal Electrodynamics and Modeling,” in *Directions in Electromagnetic*

- Wave Modeling*, H. L. Bertoni and L. B. Felsen, eds., Plenum Publishing Co., New York, 1991, pp. 435–446.
- [3] D. L. Jaggard, “Fractal Electrodynamics: Wave Interactions with Discretely Self-Similar Structures,” in *Electromagnetic Symmetry*, C. Baum and H. Kritikos, eds., Taylor & Francis, Washington, D.C., 1995, pp. 231–281.
 - [4] D. L. Jaggard, “Fractal Electrodynamics: From Super Antennas to Superlattices,” in *Fractals in Engineering: 1997*, J. L. Véhel, E. Lutton, and C. Tricot, eds., Springer-Verlag, Berlin, 1997, pp. 204–221.
 - [5] M. V. Berry, “Diffractals,” *J. Phys. A: Math. Gen.*, **12**, 781–797 (1979).
 - [6] M. V. Berry and T. M. Blackwell, “Diffractal Echoes,” *J. Phys. A: Math. Gen.*, **14**, 3101–3110 (1981).
 - [7] E. Jakeman, “Scattering by a Corrugated Random Surface with Fractal Slope,” *J. Phys. A*, **15**, L55–L59 (1982).
 - [8] E. Jakeman, “Fresnel Scattering by a Corrugated Random Surface with Fractal Slope,” *J. Opt. Soc. Am.*, **72**, 1034–1041 (1982).
 - [9] E. Jakeman, “Fraunhofer Scattering by a Sub-Fractal Diffuser,” *Optica Acta*, **30**, 1207–1212 (1983).
 - [10] E. Jakeman, “Scattering by Fractals,” in *Fractals in Physics*, L. Pietronero and E. Tosatti, eds., Elsevier Science Publishers B.V., New York, 1986, pp. 55–60. See Ref. [35].
 - [11] C. Allain and M. Cloitre, “Optical Fourier Transforms of Fractals,” in *Fractals in Physics*, L. Pietronero and E. Tosatti, eds., Elsevier Science Publishers B.V., New York, 1986, pp. 61–64. See Ref. [35].
 - [12] C. Allain and M. Cloitre, “Optical Diffraction on Fractals,” *Phys. Rev. B*, **33**, 3566–3569 (1986).
 - [13] C. Bourrelly, P. Chiappetta, and B. Torresani, “Light Scattering by Particles of Arbitrary Shape: A Fractal Approach,” *J. Opt. Soc. Am. A*, **3**, 250–255 (1986).
 - [14] C. Bourrelly and B. Torresani, “Scattering of an Electromagnetic Wave by an Irregularly Shaped Object,” *Optics Comm.*, **58**, 365–368 (1986).
 - [15] C. Allain and M. Cloitre, “Spatial Spectrum of a General Family of Self-Similar Arrays,” *Phys. Rev. A*, **36**, 5751–5757 (1987).
 - [16] D. L. Jaggard and X. Sun, “Scattering from Bandlimited Fractal Fibers,” *IEEE Trans. Ant. and Propagat.*, **37**, 1591–1597 (1989).
 - [17] M. M. Beal and N. George, “Features in the Optical Transforms of Serrated Apertures and Disks,” *J. Opt. Soc. Am. A*, **6**, 1815–1826 (1989).
 - [18] X. Sun and D. L. Jaggard, “Scattering from Fractally Fluted Cylinders,” *J. Electromagnetic Wave Appl.*, **4**, 599–611 (1990).
 - [19] Y. Kim, H. Grebel, and D. L. Jaggard, “Diffraction by Fractally Serrated Apertures,” *J. Opt. Soc. A*, **8**, 20–26 (1991).
 - [20] D. L. Jaggard, T. Spielman, and X. Sun, “Diffraction by Cantor Targets,” in *Conference Proceedings of the 1991 AP-S/URSI Meeting*, London, Ontario, 1991.
 - [21] T. Spielman and D. L. Jaggard, “Diffraction by Cantor Targets: Theory and Experiment,” in *Conference Proceedings of the 1992 AP-S/URSI Meeting*, Chicago, Illinois, 1992.
 - [22] H. D. Bale and P. W. Schmidt, “Small-Angle X-Ray-Scattering Investigation of Submicroscopic Porosity with Fractal Properties” *Phys. Rev. Lett.*, **53**, 596–599 (1984).
 - [23] D. W. Schaefer, J. E. Martin, P. Wiltzius, and D. S. Cannell, “Fractal Geometry of Colloidal Aggregates,” *Phys. Rev. Lett.*, **52**, 2371–2374 (1984).
 - [24] B. H. Kaye, J. E. L. Blanc, and P. Abbott, “Fractal Description of the Structure Fresh and Eroded Aluminum Shot Fineparticles,” *Part. Charact.*, **2**, 56–61 (1985).

- [25] P. W. Schmidt and X. Dacai, “Calculation of the Small-Angle X-Ray and Neutron Scattering From Nonrandom (Regular) Fractals,” *Phys. Rev. A*, **33**, 560–566 (1986).
- [26] D. Rojanski, D. Huppert, H. D. Bale, X. Dacai, P. W. Schmidt, D. Farin, A. Seri-Levy, and D. Avnir, “Integrated Fractal Analysis of Silica: Adsorption, Electronic Energy Transfer, and Small-Angle X-Ray Scattering,” *Phys. Rev. Lett.*, **56**, 2505–2508 (1986).
- [27] J. Teixeira, “Experimental Methods for Studying Fractal Aggregates,” in *On Growth and Form: Fractal and Non-Fractal Patterns in Physics*, H. E. Stanley and N. Ostrowsky, eds., Martinus Nijhoff Publishers, Boston, MA, 1986, pp. 145–162. See Ref. [36].
- [28] J. G. Rarity and P. N. Pusey, “Light Scattering from Aggregating Systems: Static, Dynamic (QELS) and Number Fluctuations,” in *On Growth and Form: Fractal and Non-Fractal Patterns in Physics*, H. E. Stanley and N. Ostrowsky, eds., Martinus Nijhoff Publishers, Boston, MA, 1986, pp. 218–221. See Ref. [36].
- [29] B. H. Kaye, “Fractal Dimension and Signature Waveform Characterization of Fine Particle Shape,” *American Laboratory*, pp. 55–63 (1986).
- [30] Z. Chen, P. Sheng, D. A. Weitz, H. M. Lindsay, M. Y. Lin, and P. Meakin, “Optical Properties of Aggregate Clusters,” *Phys. Rev. B*, **37**, 5232–5235 (1988).
- [31] J. G. Rarity, R. N. Seabrook, and R. J. G. Carr, “Light-Scattering Studies of Aggregation,” in *Fractals in the Natural Sciences*, M. Fleischmann, D. J. Tildesley, and R. C. Ball, eds., Princeton University Press, Princeton, NJ, 1989, pp. 89–102. See Ref. [40].
- [32] M. Y. Lin, H. M. Lindsay, D. A. Weitz, R. C. Ball, R. Klein, and P. Meakin, “Universality of Fractal Aggregates as Probed by Light Scattering,” in *Fractals in the Natural Sciences*, M. Fleischmann, D. J. Tildesley, and R. C. Ball, eds., Princeton University Press, Princeton, NJ, 1989, pp. 71–87. See Ref. [40].
- [33] S. K. Sinha, “Scattering from Fractal Structures,” *Physica D*, **38**, 310–314 (1989).
- [34] K. J. Falconer, *The Geometry of Fractal Sets*, Cambridge University Press, Cambridge, 1985.
- [35] *Fractals in Physics*, L. Pietronero and E. Tosatti, eds., Elsevier Science Publishers B.V., New York, 1986.
- [36] *On Growth and Form: Fractal and Non-Fractal Patterns in Physics*, H. E. Stanley and N. Ostrowsky, eds., Martinus Nijhoff Publishers, Boston, MA, 1986.
- [37] J. Feder, *Fractals*, Plenum Press, New York, 1988.
- [38] M. Barnsley, *Fractals Everywhere*, Academic Press, New York, 1988.
- [39] *The Science of Fractal Images*, H.-O. Peitgen and D. Saupe, eds., Springer-Verlag, New York, 1988.
- [40] *Fractals in the Natural Sciences*, M. Fleischmann, D. J. Tildesley, and R. C. Ball, eds., Princeton University Press, Princeton, NJ, 1989.
- [41] K. J. Falconer, *Fractal Geometry: Mathematical Foundations and Applications*, John Wiley and Sons, Chichester, 1990.
- [42] A. L. Méhauté, *Fractal Geometries: Theory and Applications*, CRC Press Inc., Boca Raton, 1991, originally appeared in French as *Les Géométries Fractales: L'espace-temps brisé* in 1990 by Editions Hermès, Paris.
- [43] M. Schroeder, *Fractals, Chaos, Power Laws: Minutes from an Infinite Paradise*, W. H. Freeman and Company, New York, 1991.
- [44] *Fractals and Disordered Systems*, A. Bunde and S. Havlin, eds., Springer-Verlag, Berlin, 1991.
- [45] *Fractals: Non-Integral Dimensions and Applications*, G. Cherbit, ed., John Wiley and Sons, Chichester, 1991.
- [46] G. A. Edgar, *Measure, Topology, and Fractal Geometry*, Springer-Verlag, New York, 1990.

- [47] D. L. Turcotte, *Fractals and Chaos in Geology and Geophysics*, Cambridge University Press, Cambridge, 1992.
- [48] H.-O. Peitgen, H. Jürgens, and D. Saupe, *Chaos and Fractals: New Frontiers of Science*, Springer-Verlag, New York, 1992.
- [49] T. Vicsek, *Fractal Growth Phenomena*, 2 edn, World Scientific, Singapore, 1992.
- [50] D. L. Jaggard and X. Sun, "Scattering by Fractally Corrugated Surfaces," *J. Opt. Soc. A*, **7**, 1131–1139 (1990).
- [51] X. Sun and D. L. Jaggard, "Wave Scattering from Non-Random Fractal Surfaces," *Opt. Comm.*, **78**, 20–24 (1990).
- [52] D. L. Jaggard and X. Sun, "Rough Surface Scattering: A Generalized Rayleigh Solution," *J. Appl. Phys.*, **68**, 5456–5462 (1990).
- [53] A. Dogariu, J. Uozumi, and T. Asakura, "Angular Power Spectra of Fractal Structures," *J. Mod. Optics*, **41**, 729–738 (1994).
- [54] P. McSharry and P. J. Cullen, "Wave Scattering by a One-Dimensional Band-Limited Fractal Surface Based on a Perturbation of the Green's Function," *J. Appl. Phys.*, **78**, 6940–6948 (1995).
- [55] S. Savaidis, P. Frangos, D. L. Jaggard, and K. Hizanidis, "Scattering from Fractally Corrugated Surfaces: An Exact Approach," *Opt. Lett.*, **20**, 2357–2359 (1995).
- [56] J. Chen, T. K. Y. Lo, H. Leung, and J. Litva, "The Use of Fractals for Modeling EM Waves Scattering from Rough Sea Surface," *IEEE Trans. Geo. Remote Sensing*, **34**, 966–972 (1996).
- [57] G. Franceschetti, M. Migliaccio, and D. Riccio, "An Electromagnetic Fractal-Based Model for the Study of the Fading," *Radio Sci.*, **31**, 1749–1759 (1996).
- [58] K. Ivanova and O. I. Yordanov, "Bistatic Properties of Kirchhoff Diffractals," *Radio Sci.*, **31**, 1901–1906 (1996).
- [59] C. A. Guérin, M. Holschneider, and M. Saillard, "Electromagnetic Scattering from Multi-Scale Rough Surfaces," *Waves in Random Media*, **7**, 331–349 (1997).
- [60] S. Savaidis, P. Frangos, D. L. Jaggard, and K. Hizanidis, "Scattering from Fractally Corrugated Surfaces Using the Extended Boundary Condition Method," *J. Opt. Soc. Am. A*, **14**, 475–485 (1997).
- [61] S. Rouvier and P. Borderies, "Ultra Wide Band Electromagnetic Scattering of a Fractal Profile," *Radio Science*, **32**, 285–293 (1997).
- [62] J. A. Shaw and J. H. Churnside, "Fractal Laser Glints from the Ocean Surface," *J. Opt. Soc. A*, **14**, 1144–1150 (1997).
- [63] F. Berizzi and E. D. Mese, "Fractal Analysis of the Signal Scattered from the Sea Surface," *IEEE Trans. Ant. and Propagat.*, **47**, to appear (1999).
- [64] F. Berizzi, E. D. Mese, and G. Pinelli, "A One-Dimensional Fractal Model of the Sea Surface," *Sonar and Navigation*, **146**, 55–64 (1999).
- [65] F. Berizzi and E. D. Mese, "A Fractal Theoretical Approach for the Sea Wave Spectrum Evaluation," in preparation (1998–1999).
- [66] G. Franceschetti, A. Iodice, M. Migliaccio, and D. Riccio, "Scattering from Natural Rough Surfaces Modelled by Fractional Brownian Motion Two-Dimensional Processes," *IEEE Trans. Ant. and Propagat.*, **47**, to appear (1999).
- [67] A. Collaro, G. Franceschetti, M. Migliaccio, and D. Riccio, "Gaussian Rough Surfaces and Kirchhoff Approximation," *IEEE Trans. Ant. and Propagat.*, **47**, to appear (1999).
- [68] D. L. Jaggard and X. Sun, "Reflection from Fractal Layers," *Opt. Lett.*, **15**, 1428–1430 (1990).
- [69] V. V. Konotop, O. I. Yordanov, and I. V. Yurkevich, "Wave Transmission Through a

- One-Dimensional Cantor-Like Fractal Medium,” *Europhys. Lett.*, **12**, 481–485 (1990).
- [70] X. Sun and D. L. Jaggard, “Wave Interactions with Generalized Cantor Bar Fractal Multi-Layers,” *J. Appl. Phys.*, **70**, 2500–2507 (1991).
- [71] T. Megademi, B. Pardo, and R. Jullien, “Fourier Transform and Theory of Fractal Multilayer Mirrors,” *Opt. Comm.*, **80**, 312–316 (1991).
- [72] M. Bertolotti, P. Masciulli, and C. Sibilia, “Spectral Transmission Properties of a Self-Similar Optical Fabry-Perot Resonator,” *Opt. Lett.*, **19**, 777–779 (1994).
- [73] S. De Nicola, “Reflection and Transmission of Cantor Fractal Layers,” *Opt. Comm.*, **111**, 11–17 (1994).
- [74] S. A. Bulgakov, V. V. Konotop, and L. Vázquez, “Wave Interaction with a Random Fat Fractal: Dimension of the Reflection Coefficient,” *Waves in Random Media*, **5**, 9–18 (1995).
- [75] D. L. Jaggard and A. D. Jaggard, “Polyadic Cantor Superlattices with Variable Lacunarity,” *Opt. Lett.*, **22**, 145–147 (1997).
- [76] A. D. Jaggard and D. L. Jaggard, “Fractal Superlattices and Scattering: Lacunarity, Fractal Dimension, and Stage of Growth,” in *Conference Proceedings of the 1997 AP-S/URSI Meeting*, Montréal, Canada, 1997.
- [77] A. D. Jaggard and D. L. Jaggard, “Scattering from Fractal Superlattices with Variable Lacunarity,” *J. Opt. Soc. Am. A*, **15**, 1626–1635 (1998).
- [78] B. B. Mandelbrot, *The Fractal Geometry of Nature*, Freeman, San Francisco, 1983.
- [79] C. Allain and M. Cloitre, “Characterizing the Lacunarity of Random and Deterministic Fractal Sets,” *Phys. Rev. A*, **44**, 3552–3558 (1991).
- [80] D. L. Jaggard and Y. Kim, “Diffraction by Bandlimited Fractal Screens,” *J. Opt. Soc. Am. A*, **4**, 1055–1062 (1987).
- [81] P. Beckmann and A. Spizzichino, *The Scattering of Electromagnetic Waves from Rough Surfaces*, Pergamon, New York, 1963.
- [82] J. Uozumi, H. Kimura, and T. Asakura, “Fraunhofer Diffraction by Koch Fractals: The Dimensionality,” *J. Mod. Optics*, **38**, 1335–1347 (1991).
- [83] D. L. Jaggard and A. D. Jaggard, “Fractal Apertures: The Effect of Lacunarity,” in *Conference Proceedings of the 1997 AP-S/URSI Meeting*, Montréal, Canada, 1997.
- [84] D. L. Jaggard and A. D. Jaggard, “Cantor Ring Arrays,” in *Conference Proceedings of the 1998 AP-S/URSI Meeting*, Atlanta, GA, 1998.
- [85] D. L. Jaggard and A. D. Jaggard, “Fractal Arrays and Lacunarity,” in *Proceedings of PIERS'98*, Nantes, France, 1998.
- [86] D. L. Jaggard and A. D. Jaggard, “Fractal Ring Arrays,” invited paper submitted to *Wave Motion* (1999).
- [87] G. Franceschetti, M. Migliaccio, and D. Ricci, “Scattering from Natural Surfaces via a Two-scale Fractal Model,” in *Proceedings of the URSI International Symposium on Electromagnetic Theory*, pp. 685–687, St. Petersburg, Russia, 1995.
- [88] G. Franceschetti, M. Migliaccio, and D. Ricci, “Fractal Modelling of Microscopic Roughness Scattering,” in *Proceedings of the URSI International Symposium on Wave Propagation and Remote Sensing*, pp. 160–163, Ahmedabad, India, 1995.
- [89] G. Franceschetti, M. Migliaccio, and D. Ricci, “A Fractal-Based Approach to Electromagnetic Modelling,” in *Proceedings of IGARSS'94*, pp. 1641–1643, Pasadena, CA, 1996.
- [90] F. Berizzi and E. D. Mese, “Fractal Theory of Sea Fractal Scattering,” in *Proceedings of 1996 CIE International Conference of Radar*, pp. 661–665, Beijing, China, 1996.
- [91] G. Andreoli, F. Berizzi, E. D. Mese, and G. Pinelli, “Fractal Model of the Sea Surface and Statistical Analysis of the Sea-Scattered Signal,” in *Proceedings of the Fractals in*

- Engineering Conference*, Arcachon, France, 1997.
- [92] G. Andreoli, F. Berizzi, E. D. Mese, and G. Pinelli, "A Two-Dimensional Fractal Model of the Sea Surface and Sea Spectrum Evaluation," in *Proceedings of the IEE International Radar Conference*, pp. 189–193, Edinburgh, Scotland, 1997.
 - [93] G. Franceschetti, M. Migliaccio, and D. Ricci, "Fractal Models of Scattering from Natural Bodies," in *Proceedings of PIERS'97*, p. 74, Hong Kong, 1997.
 - [94] G. Franceschetti, A. Iodice, M. Migliaccio, and D. Ricci, "Backscattering from an fBm Surface," in *Proceedings of the URSI International Symposium on Electromagnetic Theory*, pp. 692–694, Thessaloniki, Greece, 1998.
 - [95] G. Franceschetti, A. Iodice, M. Migliaccio, and D. Ricci, "Scattering from Natural Rough Surfaces Described by the fBm Fractal Model," in *Proceedings of PIERS'98*, p. 1153, Nantes, France, 1998.
 - [96] G. Andreoli, F. Berizzi, E. D. Mese, and G. Pinelli, "A Two-Dimensional Fractal Model of the Sea Surface and Sea Spectrum Evaluation," in *Proceedings of IGARSS '98*, Seattle, Washington, 1998.
 - [97] P. C. Waterman, "Matrix Formulation of Electromagnetic Scattering," *Proc. IEEE*, **53**, 805–812 (1965).
 - [98] P. C. Waterman, "Symmetry, Unitarity, and Geometry in Electromagnetic Scattering," *Phys. Rev., D*, **3**, 825–839 (1971).
 - [99] P. C. Waterman, "Scattering by Periodic Surfaces," *J. Acoust. Soc. Am.*, **57**, 791–802 (1975).
 - [100] S. L. Chuang and J. A. Kong, "Scattering of Waves from Periodic Surfaces," *Proc. IEEE*, **69**, 1132–1144 (1981).
 - [101] J. A. Sanchez and M. Nieto-Vesperinas, "Light Scattering from Random Rough Dielectric Surfaces," *J. Opt. Soc. Am. A*, **8**, 1270–1286 (1991).
 - [102] J. A. Kong, *Electromagnetic Wave Theory*, John Wiley & Sons, New York, 1986.
 - [103] A. Ishimaru, *Electromagnetic Wave Propagation, Radiation, and Scattering*, Prentice Hall, Englewood Cliffs, NJ, 1991.
 - [104] A. R. Mickelson and D. L. Jaggard, "Electromagnetic Wave Propagation in Almost-Periodic Media," *IEEE Trans. Ant. and Propagat.*, **AP-27**, 34–40 (1979).
 - [105] Z. Knittl, *Optics of Thin Films (An Optical Multilayer Theory)*, John Wiley & Sons, London, 1976.
 - [106] A. D. Jaggard and D. L. Jaggard, "Cantor Superlattices: Extracting Fractal Descriptors," in preparation for publication (1999).
 - [107] A. D. Jaggard and D. L. Jaggard, "Fractal Superlattices: A Frequency Domain Approach," in *Proceedings of PIERS'98*, Nantes, France, 1998.
 - [108] Y. Kim and D. L. Jaggard, "Wave Interactions with Continuous Fractal Layers," in *Proceedings of the 1991 SPIE Meeting vol. 1558*, pp. 113–119, John Wiley & Sons, San Diego, 1991.
 - [109] H. Aubert and D. L. Jaggard, "Fractal Superlattices and Their Wavelet Analyses," *Opt. Comm.*, **149**, 207–212 (1998).
 - [110] H. Aubert and D. L. Jaggard, "Wavelet Analysis of Transients in Fractal Superlattices," to appear in *IEEE Trans. Ant. and Propagat.*, (1999–2000).
 - [111] I. Daubechies, *Ten Lectures on Wavelets*, S.I.A.M., Philadelphia, 1992.
 - [112] A. Dogariu, J. Uozumi, and T. Asakura, "Wavelet Transform Analysis of Slightly Rough Surfaces," *Optics Comm.*, **107**, 1–5 (1994).
 - [113] H. Aubert and D. L. Jaggard, "Continuous Wavelet Transform Analysis of Fractal Superlattices," in *Fractals: Theory and Applications in Engineering*, M. Dekking, J. Lévy Véhel, E. Lutton, and C. Tricot, eds., Springer, London, 1999, pp. 245–259.